

# Fine Scale Temperature Fluctuations in the the Orion Nebula and the $t^2$ Problem <sup>1</sup>

C. R. O'Dell

*Department of Physics and Astronomy, Vanderbilt University, Box 1807-B, Nashville, TN 37235*

`cr.odell@vanderbilt.edu`

Manuel Peimbert

*Instituto de Astronomía, Apartado Postal 70-264, UNAM, Mexico City, DF 004510 México*

Antonio Peimbert

*Instituto de Astronomía, Apartado Postal 70-264, UNAM, Mexico City, DF 004510 México*

## ABSTRACT

We present a high spatial resolution map of the columnar electron temperature ( $T_e$ ) of a region to the south west of the Trapezium in the Orion Nebula. This map was derived from Hubble Space Telescope images that isolated the primary lines of H I for determination of the local extinction and of the [O III] lines for determination of  $T_e$ . Although there is no statistically significant variation of  $T_e$  with distance from the dominant ionizing star  $\theta^1$  Ori C, we find small scale variations in the plane of the sky down to a few arcseconds that are compatible with the variations inferred from comparing the value of  $T_e$  derived from forbidden and recombination lines, commonly known as the  $t^2$  problem. We present other evidence for fine scale variations in conditions in the nebula, these being variations in the surface brightness of the the nebula, fluctuations in radial velocities, and ionization changes. From our  $T_e$  map and other considerations we estimate that  $t^2 = 0.028 \pm 0.006$  for the Orion nebula. Shadowed regions behind clumps close to the ionization front can make a significant contribution to the observed temperature fluctuations, but they cannot account for the  $t^2$  values inferred from several methods of temperature determination. It is shown that an anomalous broadening of nebular emission lines appears to have the same sense of correlation as the temperature anomalies, although a causal link is not obvious.

*Subject headings:* ISM:H II Regions–ISM:abundances–ISM:individual(Orion Nebula)

## 1. Introduction

Photoionization models for chemically homogeneous gaseous nebulae of constant density predict an almost constant temperature; consequently, observers often assume a constant temperature to determine chemical abundances. The spatial temperature inhomogeneities in H II regions are usually characterized by  $t^2$  the mean square temperature variation in three dimensions. Recent reviews on the temperature structure of gaseous nebulae are those by Peimbert (1995, 2002), Esteban (2002), Stasińska (2002), Liu (2002), Torres-Peimbert & Peimbert (2003).

From uniform-density chemically-homogeneous photoionization models it has been found that  $t^2$  is in the 0.002 to 0.025 range, for objects with solar or subsolar chemical abundances, with typical values around 0.005 (e.g., Gruenwald & Viegas 1992, Garnett 1992). Baldwin et al. (1991, henceforth B91) produced a photoionization model for the Orion Nebula, in which grains and gas are well mixed, that included photoelectric heating and cooling of the gas by grain ionization and grain collisions respectively; for this model Peimbert, Storey, & Torres-Peimbert (1993) found that  $t^2 = 0.004$ .

Alternatively from observations of NGC 346 in the SMC (Peimbert, Peimbert, & Ruiz 2000), 30 Doradus (Peimbert 2003), and the Orion Nebula (Peimbert et al. 1993, Esteban et al. 1998, henceforth EPTE98) it has been found that  $t^2$  is in the 0.02 to 0.04 range. The  $t^2$  values were derived by combining the temperature derived from the ratio of the [O III]  $\lambda\lambda$  4363, 5007 lines [ $T_{(4363/5007)}$ ] with the temperature derived from the ratio of the Balmer continuum to  $I(H\beta)$  [ $T_{(Bac/H\beta)}$ ] and by combining  $T_{(4363/5007)}$  with the temperatures derived from the ratio of  $\lambda$  5007 to the recombination lines of multiplet 1 of O II and the ratio of the of  $\lambda\lambda$  1906, 1909 [C III] lines to the  $\lambda$  4267 C II recombination line.

The differences between the observed  $t^2$  values and those predicted by models have two profound implications for the study of ionized gaseous Nebulae: they significantly affect the derived abundances and they imply the presence of one or several physical mechanisms not considered by the models.

To study this problem further we decided to obtain an independent measurement of  $t^2$  based on over a million temperatures determined across the face of the Orion nebula. The subarcsecond resolution of the HST makes it ideal for this purpose. Each of these temperatures represents an average along a given line of sight. Since the columnar temperatures

---

<sup>1</sup>Based in part on observations with the NASA/ESA Hubble Space Telescope, obtained at the Space Telescope Science Institute, which is operated by the Association of Universities for Research in Astronomy, Inc., under NASA Contract No. NAS 5-26555.

already represent an average temperature it is not possible to obtain directly from them the full  $t^2$  value. Instead it is possible to obtain the mean square temperature variation across the plane of the sky and from this value it is possible to estimate  $t^2$ .

In § 2 we discuss the observations. In § 3 and § 4 we present the method for deriving the columnar temperature ( $T_c$ ) image together with its analysis. In § 5 we formally define the columnar temperature, and the mean square temperature variation measured in the plane of the sky ( $t_A^2$ ), then determine  $t_A^2$  from the [O III] data. We then estimate  $t^2$  based on  $t_A^2$  and additional data from the  $T_c$  image and [N II] temperatures. In § 6 we compare our results with those of previous work. A new model for the structure of the Nebula near the ionization front is presented in § 7. Finally, the conclusions are presented in § 8.

## 2. The Observations

The intent of this observational program was to establish accurate [O III] 4363 Å and 5007 Å line ratios across the Orion Nebula using the WFPC2 camera (Holtzman et al. 1995) of the Hubble Space Telescope (HST) and its narrow-band interference filters. This required imaging the nebula in the filters intended to isolate these lines (F437N and F502N, respectively). Since the extinction varies at small scales across the face of the nebula (O’Dell & Yusef-Zadeh 2000), the magnitude of the extinction was determined on the same size scale as the [O III] line observations. This required determination of the H $\alpha$  and H $\beta$  line ratios, which demanded observations with the F656N and F487N filters. Since the former filter allows some emission from the nearby [N II] doublet to contaminate the H $\alpha$  signal, it was also necessary to observe with the F658N filter, which is dominated by the [N II] 6583 Å line. There was the possibility of the H $\gamma$  line contaminating the F437N signal. The anticipation was that this could be handled by scaling from the H $\beta$  observations in F487N. Each emission line filter also passes the nebular continuum radiation. In the case of the emission line signal being very strong as compared with the underlying continuum it is sufficient to measure the visual continuum with the F547M filter and extrapolate to the wavelength of the emission line filter (O’Dell & Yusef-Zadeh 2000, O’Dell 1998a). However, the continuum of the Orion Nebula is quite strong (O’Dell & Hubbard 1965, B91) because the large optical depth of dust particles lying just beyond the main ionization front (MIF) back-scatter a significant fraction of the visual starlight reaching it. This back-scatter produces a continuum much stronger than that arising from atomic processes. The observations most sensitive to continuum contamination are those of the intrinsically weak 4363 Å line. Fortunately, the F469N filter provided a good measure of the strength of the local continuum because it is free of strong emission lines when used to observe a low ionization object like the

Orion Nebula. It is known that the He II 4686 Å line (which the F469N filter was designed to isolate in high ionization objects) is undetected in the Orion Nebula even in spectroscopic studies reaching nearly  $10^{-4}$  the intensity of H $\beta$  (B91, EPTE98). Combining the F547M and F469N observations allowed a linear extrapolation or interpolation of the wavelength dependence of the continuum flux to the wavelength of each filter. The filters employed and their pre-launch characteristics (WFPC2 Instrument Handbook, version 6.1 available at <http://www.stsci.edu>) are summarized in Table 1. This table also gives the WFPC2+HST system throughput as recently determined in orbit.

Because of the host of filters that had to be used and the length of the observing times necessary for producing an adequate signal in the fainter lines, only one field of view was covered. This was selected to include regions that had been spectroscopically studied recently using high dynamic range detectors (B91 and EPTE98), in order to allow a precise calibration of the filters, and to avoid the presence of the bright Trapezium stars. As will be noted in § 3.3, the brightest Trapezium star ( $\theta^1$  Ori C) was so close ( $7''$ ) to the CCD1 detector that low-level scattered light problems affected the long exposure images with that detector, rendering them useless for this program. The [O III] image is shown in Figure 1. The four CCD detectors of the WFPC2 are numbered counter-clockwise, with the high-angular resolution, but smaller field of view, CCD being designated as CCD1.

All exposures were made with exactly the same pointing on 2002 January 21, 22, and 26 and at the same gain (electrons/ADU) values. Multiple exposures of the same duration were made with each filter in order to allow correction for cosmic ray induced events on the detectors. The individual exposure times and number of exposures were: F437N(1100 s, 6x), F469N(1100 s, 6x), F487N(350 s, 3x), F502N(160 s, 3x), F547M(230 s, 3x), F656N(140 s, 2x), F658N(200, 2x). All images were “on-the-fly” calibrated by the Space Telescope Science Institute (STScI) and then processed using their STSDAS and the National Optical Astronomy Observatories IRAF <sup>2</sup> tasks. The final product of the routine processing was a combined image such as shown in Figure 1.

### 3. Derivation of the $T_c$ Image

A considerable number of steps were necessary to convert the photometric observations with WFPC2 into [O III] 4363 Å and 5007 Å line ratios and from these line ratios into  $T_c$

---

<sup>2</sup>IRAF is distributed by the National Optical Astronomy Observatories, which is operated by the Association of Universities for Research in Astronomy, Inc. under cooperative agreement with the National Science foundation.

values. In this section we first describe the method of calibration of the filter properties and other components of the photometric system and their application to obtaining line ratios. We then describe the method of correcting for interstellar reddening. Finally, we derive the pixel by pixel values of  $T_c$  and estimate the statistical noise of the  $T_c$  values.

### 3.1. Method of Calibration of the Filters

The method of calibration adopted was identical to that employed by O’Dell & Doi (1999, henceforth OD99). However, in the present case we are only interested in the relative line fluxes, so that their equations for an absolute calibration can be simplified. The reader interested in absolute calibrations should refer to OD99, but note that an editing error occurs in their equation (5). The term that reads  $N_{658}t_{656}T_{N II}^{656}$  should read  $N_{658}t_{656}T_{H\alpha}^{656}$ , this error does not affect any of the numerical results in that paper. The basic approach is that one uses the WFPC2 observations of spectroscopically well studied regions to determine the calibration constants, which can then be applied to all the pixels of the image since the filter profile and system sensitivity does not vary across the image (after the appropriate flat-field corrections have been applied). The most important calibration constants are determined directly from the observations of the reference regions and only the secondary constants draw on filter characteristics that were last determined before launch of the WFPCs. Since the filter and detector characteristics can change with time, this method of calibration permits accurate determination of the most important characteristics.

Our method of deriving relative calibrations relates  $N_{\text{filter}}$  (the recorded number of ADU counts per unit time) to the characteristics of the source and the filter and camera system through the equation

$$N_{\text{filter}} = \sum s_{\text{line}} T_{\text{line}}^{\text{filter}} S_{\text{line}} + s_{\text{cont}} E_{\text{filter}} S_{\text{cont}}^{\text{filter}}, \quad (1)$$

where we have used the following nomenclature:

$s_{\text{line}}$ =system throughput of the telescope-camera-detector system for a particular line (excluding the filter)

$T_{\text{line}}^{\text{filter}}$ =transmission at a particular line of a filter

$S_{\text{line}}$ =surface brightness of a particular line in photons  $\text{cm}^{-2}\text{s}^{-1}\text{ster}^{-1}$

$s_{\text{cont}}$ =system throughput of the telescope-camera-detector system for the continuum (excluding the filter)

$E_{\text{filter}} = \int_0^\infty T_\infty d\lambda$ =effective width of the filter in  $\text{\AA}$

$S_{\text{cont}}^{\text{filter}}$  = surface brightness of the continuum in photons  $\text{cm}^{-2}\text{s}^{-1}\text{ster}^{-1}\text{\AA}^{-1}$ .

It is important to note that this calibration is done in units of the number of photons. When necessary, the resulting numbers can be converted to the relative flux. In this program multiple lines contributed to the signal from a single filter only in the case of F656N ( $\text{H}\alpha$ -6563  $\text{\AA}$ ,  $[\text{N II}]$ -6548  $\text{\AA}$ +6583  $\text{\AA}$ ) and F658N ( $[\text{N II}]$ -6583  $\text{\AA}$ ,  $\text{H}\alpha$ -6563  $\text{\AA}$ ). We considered the contribution of  $\text{H}\gamma$  4340 to the F437N filter, but found it to be negligible.

The reference regions were all taken from B91. They observed with a long slit of east-west orientation located to the east of  $\theta^1$  Ori C. The exact location was incorrectly expressed in B91, but is correctly described in OD99. B91 gives line ratios and continuum to  $\text{H}\beta$  ratios for 21 samples along their slit. We used the six samples that overlapped with the CCD4 portion of our images (shown in Figure 1) that included 4363  $\text{\AA}$  relative intensities. Each sample was  $2'' \times 15.76''$  in size.

The results of this calibration gave the following equations for the two important line ratios,  $\text{H}\alpha/\text{H}\beta$  and 4363/5007.

$$\frac{S_{\text{H}\alpha}}{S_{\text{H}\beta}} = 0.443 \frac{N_{656}}{N_{487}} \frac{[1 - 0.17 \frac{N_{658}}{N_{656}} (1 + 0.19 \frac{N_{547}}{N_{658}})]}{(1 - 1.28 \frac{N_{469}}{N_{487}})}, \quad (2)$$

and

$$\frac{S_{4363}}{S_{5007}} = 1.90 \frac{N_{437}}{N_{502}} \frac{[1 - 0.787 \frac{N_{469}}{N_{437}} (74.3 \frac{N_{469}}{N_{547}} - 0.28)]}{[1 - 1.62 \frac{N_{469}}{N_{502}} (33.4 \frac{N_{469}}{N_{547}} + 0.423)]}. \quad (3)$$

Equation (2) uses a full-image average value for the color of the continuum and scales the continuum intensity from the closer continuum filter. Equation (3) derives the color of the continuum at each pixel and then extrapolates or interpolates from the two continuum filters, this step being necessary as the continuum correction is quite important in the F437N measurements. The continuum typically contributes about 73% of the total signal in the F437N filter.

In a similar investigation of planetary nebulae Rubin et al. (2002, henceforth R2002) argued that there should be a small correction in the F437N filter for contamination in the blueward wing by  $\text{H}\gamma$  4340  $\text{\AA}$  emission. If one takes the pre-launch transmission profiles in the Instrument Handbook at face value, this would seem to be the case. However, it

must be expected that the profiles of the filters change as they age in space. These changes are why we wanted to calibrate our observations within the data set. One would expect that the transmission near the principal lines to not change much with time, since they are located near the peak of the filters’ transmissions, whereas the H $\gamma$  line falls far out on the wing of the filter curve. The Instrument Handbook indicates that the CCD sensitivities and throughput of the system have been remarkably constant. This combination of factors allowed us to empirically search for evidence of H $\gamma$  contamination. We could determine the ratio  $s_{437}T_{4363}^{437}/s_{487}T_{4861}^{487}$  with and without a correction for H $\gamma$  contamination. With the correction the ratio was 0.42 and without the correction the ratio was 0.68. The Instrument Handbook values indicate an expected value for the ratio of 0.62. This indicates that the correction to the 4363 Å line surface brightness for H $\gamma$  is about 10%. Since the method of calibration essentially forces the calibration constants to be such as to give the right intensity ratios for the lines assumed to be present, this means that the effects of H $\gamma$  correction will only enter in regions where the [O III] line and the H $\gamma$  line vary considerably in relative intensity. This is not the case for the area covered by the present images (B91, EPTE98).

The scatter of results from the six different samples in the calibration region indicates that the uncertainty of the Balmer line ratios will be 7%, while that of the [O III] line ratios will be about 12%. Since the reddening corrections between 4363 Å and 5007 Å are small, the effects of the absolute uncertainty of the Balmer line ratios are negligible. A 12% systematic uncertainty of the [O III] line ratios would make the derived  $T_c$  values be off systematically by  $\pm 350$  K. This will not significantly affect our search for fine scale variations in  $T_c$ . As we will see in § 3.3, there is excellent agreement between the electron temperatures derived in B91 and those derived in this study.

### 3.2. Derivation of Extinction Corrections

The extinction corrections are based on determining the Balmer line ratio for each pixel and then calculating the total extinction from comparison with the intrinsic ratio. This total extinction was then used to correct the [O III] line ratios. We assumed with EPTE98 that the intrinsic Balmer line flux ratio was 2.91. Using the same extinction law as EPTE98 means that the extinction corrected ( $I$ ) flux ratios could be calculated from the observed flux ratios ( $F$ ) by the relation

$$\log \frac{I_{4363}}{I_{5007}} = \log \frac{F_{4363}}{F_{5007}} + 0.362 \log \frac{F_{H\alpha}}{F_{H\beta}} - 0.168. \quad (4)$$

The extinction values derived from the Balmer line ratios are in good agreement with those of O’Dell & Yusef-Zadeh (2000), this being the case for both their results obtained from radio continuum to  $H\alpha$  ratios and those obtained from their Balmer line ratios.

### 3.3. Derivation of $T_c$ Images

The [O III] reddening corrected line ratios were then used to derive local values of  $T_c$ . A convenient formulation of the relation of line ratio and  $T_c$  is given in R2002. Their equation (8) can be restated as

$$T_c = 32,966 / (\ln \frac{I_{5007}}{I_{4363}} - 1.701), \quad (5)$$

where we have restated the relation using the common-usage designation of the wavelengths in air (rather than the more physically meaningful vacuum wavelengths employed by R2002). Since we are dealing with large numbers that are not usually determined to high precision, we sometimes will express  $T_c$  by the frequent nomenclature  $T_4 \equiv T_c / 10,000$ . The resulting image is shown in Figure 2.

Figure 2 shows multiple features. The most common are the “scars” that result from stars. These continuum sources are often saturated on some of the images used to derive  $T_c$ . Even when they are not saturated, the formal value of  $T_c$  at the star positions is subject to big uncertainties owing to the multiple subtractions that occur in the derivation. Within CCD1 there are multiple features that are related to scattered light from  $\theta^1$  Ori C and the more westward members of the Trapezium. Any apparent fluctuation in  $T_c$  within CCD1 is suspect as being an artifact. There are a few features characterized by very low values of  $T_c$ , which are discussed in § 4.3.

This derivation gives for the six sample regions from the B91 study  $\langle T_4 \rangle = 0.92 \pm 0.01$ , while values given in B91 for the same samples gives  $\langle T_4 \rangle = 0.91 \pm 0.02$ . A comparison with the EPTE98 study is not possible because only their position 2 fell within a part of our image that was not useful as it fell within CCD1 and their position 1 was north of our field.

### 3.4. Expected statistical noise and its effect on $T_c$

It is important to assess the effect of the expected Poisson noise on the determination of  $T_c$  because of the low signal level in some of the filters. In the region that was used for



calibration the total number of recorded electrons ( 7 times the number of ADU’s recorded per pixel) for the key filters were F437N(1260), F469N(1260), F547M(8400), and F502N(10500). In the following discussion, we’ll assume that the root mean square deviation of a signal  $N$  is  $N^{1/2}$ . This is what we will mean as the probable error (p.e.). We will assume that for multiplicative factors the p.e.’s add quadratically. Unfortunately, one cannot determine the p.e. directly from the observations since the nebula is intrinsically variable in surface brightness.

An assessment of the p.e. per pixel was done by creating noisy images (using IRAF task *mknoise*) of the appropriate noise level for each of the observationally determined components of equation (3), then determining the p.e. of the resulting image. The p.e. was 20%. In most of the following discussions we will assume this uncertainty.

Equation (5) was then used to determined the effect of uncertainties of the [O III] line ratio on the derived value of  $T_c$ . A 20% photometric p.e. produces a p.e. in  $T_c$  of 5.7%. Throughout this paper we will present uncertainties as probable errors (p.e.) calculated as the reciprocal of the root-mean square deviation of the recorded signal.

### 3.5. The Effect of Contamination by weak [Fe III] and He I lines

The assumptions used in § 3.1 for the derivation of Eq. 3 are not fully justified since there are two weak lines that affect the signal in the more important continuum filter, F469N. The [Fe III] line appears at 4702 Å and the He I line at 4713 Å, where the transmissions are 0.51 and 0.15, respectively. As we will demonstrate in this section, the effect of these lines is small in determination of  $T_c$  in the nebula.

The presence of these weak lines will make the continuum at F469N appear brighter than it is. If we call the enhanced signal in the F469N  $N_{\text{OBS}}$  and the signal that would be observed if there were only continuum radiation  $N_{\text{CONT}}$ , then their ratio will be given by

$$\frac{N_{\text{OBS}}}{N_{\text{CONT}}} = 1 + \frac{T_{4702}^{\text{F469N}}}{E_{\text{F469N}}} \frac{S_{4702}}{S_{\text{CONT,F469N}}} + \frac{T_{4713}^{\text{F469N}}}{E_{\text{F469N}}} \frac{S_{4713}}{S_{\text{CONT,F469N}}}. \quad (6)$$

The strength of the continuum is usually measured with respect to the  $H\beta$  line at 4861 Å. This was done in B91, where their figure 2 presents a quantity which is related to the equivalent width ( $W_{H\beta}$ ) by  $\lambda/W_{H\beta}$ . The average value of their plotted quantity is 9.5, which gives an average  $W_{H\beta} = 510$  Å, which is in good agreement with earlier filter photometry over a

wide range of the nebula (O’Dell & Hubbard 1965) which showed that  $W_{H\beta}$  is nearly constant in the inner region of the nebula, then decreases outward. Having values of  $W_{H\beta}$  allows us to express the observed-quantity ratios of equation (6) as  $S_{4702}/S_{\text{CONT},F469N}=W_{H\beta}S_{4702}/S_{H\beta}$  and  $S_{4713}/S_{\text{CONT},F469N}=W_{H\beta}S_{4713}/S_{H\beta}$ . Making this substitution and inserting the known values allows the restating of equation (6) as

$$\frac{N_{\text{OBS}}}{N_{\text{CONT}}} = 1 + 14.95 \frac{S_{4702}}{S_{H\beta}} + 4.397 \frac{S_{4713}}{S_{H\beta}}. \quad (7)$$

If the ratio of line intensities with respect to  $H\beta$  are constant across the region observed, then there is no net effect, since they will be constant in the calibration region and their affects will cancel out. However, if the line ratios vary, there will be an effect on the derived line ratios. Anticipating that this effect is small, we address only the effect on equation (3). Since the correction term in the denominator of that equation is only about 0.015, we can demonstrate adequately the effect of varying contaminating line strengths by considering only the terms in the numerator. If  $(N_{\text{OBS}} / N_{\text{CONT}})_{\text{CALIB}}$  is the value of the ratio of these quantities in the region used for calibration, we can express the local effect by multiplying the N469 rates by  $(N_{\text{OBS}} / N_{\text{CONT}}) / (N_{\text{OBS}} / N_{\text{CONT}})_{\text{CALIB}}$ . The global average values (taken from a section of CCD2 free of the peculiar effects due to shocks that are discussed in § 4.2 are  $N_{437}/N_{502}= 0.0094$ ,  $N_{469}/N_{437}=1.04$ , and  $N_{469}/N_{547}=0.016$ . Inserting these values into the numerator of equation (3) and applying a constant correction of 0.015 for the subtractive term in the denominator, gives

$$\frac{S_{4363}}{S_{5007}} = 0.0181 \left\{ 1 - 0.819 \left( \frac{N_{\text{OBS}}}{N_{\text{CONT}}} \right) \left( \frac{N_{\text{CONT}}}{N_{\text{OBS}}} \right)_{\text{CALIB}} \left[ 1.19 \left( \frac{N_{\text{OBS}}}{N_{\text{CONT}}} \right) \left( \frac{N_{\text{CONT}}}{N_{\text{OBS}}} \right)_{\text{CALIB}} - 0.28 \right] \right\}. \quad (8)$$

The weak contaminating lines are seen only at high spectral resolution. In the study of Osterbrock, Tran, & Veilleux (1992), fluxes relative to  $H\beta$  were 0.00245 and 0.00686 for 4702 and 4713 respectively (for an east-west region 47" long centered 58" north of  $\theta^1$  Ori C). EPTE98 found ratios of 0.00179 and 0.00645 for a region 45" north of  $\theta^1$  Ori C and 0.00186 and 0.00621 for a region 25" south and 10" west of  $\theta^1$  Ori C. These three samples would indicate values of  $N_{\text{OBS}} / N_{\text{CONT}}$  of 1.066, 1.056, and 1.055 respectively. The contaminating lines were not measured in B91 due to their lower spectra resolution.

There is another set of data that provide even more information. Co-authors Antonio

and Manuel Peimbert together with María Teresa Ruiz obtained a long slit spectrum with the VLT3 telescope (Melipal) and the FORS1 spectrograph at the Paranal observatory in Chile on 2002 September 10. The slit was oriented at a position angle of  $340^\circ$  and passed through the feature called HH 202-S in O’Dell et al.1997 (henceforth O97) and designated in Figure 2. To estimate the intensity of the [Fe III] 4702 Å line, they measured the intrinsically stronger [Fe III] line at 4658 Å and we scaled it to the 4702 intensity by using the line ratio of 0.32 from EPTE98. Likewise, they also measured the strength of the 4713 Å feature, a blend of [Ar IV] line at 4711 Å and the He I at 4713 Å the [Ar IV] line contributing about 15% of the blend intensity. The average of a 2' section, which is close to the east-west calibration samples from B91, gave ratios relative to H $\beta$  of 0.0061 and 0.0060 for 4702 and 4713 respectively, giving a value of  $N_{\text{OBS}} / N_{\text{CONT}}=1.0551$ . The scatter of this value, taken from six 20'' subsamples was  $\pm 0.0064$ . A similar scatter was found from an analysis of both 20'' and 2'' samples.

Recalling that the effect of this 5% level contamination cancels out in our calibration procedure leaves us only to consider the effect of the variation in the value of  $T_c$  due to the varying level of contamination. The variations in contamination indicated by the Paranal data indicate that the corresponding variations in the derived  $T_c$  is +80 and -120 K.

#### 4. Analysis of the $T_c$ Image

The “temperature image” can be used to look for variations in  $T_c$  at large and fine scales. In this section we describe the results of a search for systematic changes, and explain the regions of apparently very low and high values of  $T_c$ . We also present the evidence for small scale changes, and give the results of a Fourier analysis of the temperature fluctuations.

##### 4.1. Global Variation of $T_c$ with Distance from $\theta^1$ Ori C

We looked for variations of  $T_c$  with distance from the dominant ionizing star  $\theta^1$  Ori C. Nine samples of 10''x10'' were taken from each of CCD2-4. In each case there were no scars from bright stars and none of the low  $T_c$  regions discussed in the next section. The average gave  $\langle T_c \rangle = 8890 \pm 496$  K. No statistically significant correlation was found when trying to fit a linear relation to the observed values of  $T_c$  and distance from  $\theta^1$  Ori C. We conclude that there are real variations in  $T_c$  across the region sampled in this study, but there is no obvious relation to the position in the nebula. The scatter of 496 K is significant since the scatter due to Poisson statistics within each sample would be only 5 K and we estimated

in § 3.5 that the scatter due to variations in the contaminating weak lines would be about  $\pm 100$  K.

#### 4.2. Anomalous “Low $T_c$ ” Regions

There are several regions within CCD2-CCD3-CCD4 that have anomalously low values of the derived  $T_c$ , as seen in Figure 2. These all fall within the province of known Herbig-Haro (HH) objects HH 202 (Cantó et al. 1980, O97) and HH 269 (Walter et al. 1995, Bally, O’Dell, & McCaughrean 2000). The former is probably the result of a pre-Main Sequence star’s blueshifted jet striking the foreground veil of neutral material (O97). The latter is probably the result of blueshifted jet outflow from a pre-Main Sequence star that lies behind the MIF and has yet to be identified (O’Dell & Doi 2003). It is almost certain that HH 269 has the same source as that producing the series of shocks extending to the east and designated as HH 529 (Bally, O’Dell, & McCaughrean 2000) and it is likely (O’Dell & Doi 2003) that this is also the source for the jets producing HH 202 and the double object HH 203+HH 204 that lies to the southeast, near  $\theta^2$  Ori A.

These anomalously low  $T_c$  features are probably not real, rather, they are the result of contamination of the F469N filter. Our method of calculation of the line ratios assumed that the F469N filter was free of any emission lines, i.e. it was used as a measure of the continuum. In all of the nebula for which spectra exist this assumption is good since the star producing most of the ionization of the nebula ( $\theta^1$  Ori C) is too cool to doubly ionize helium and there are only the two weak contaminating lines (c.f. § 3.5). Hartigan (1999) has shown that if a fast jet forms a bow shock in material that is already photoionized then one can expect He II to be present. He used ground based images to look for evidence for emission in the He II 4686 Å line. The only region where he thought that this line was present was in HH 202, but with his low resolution images he could not conclude that 4686 Å emission was present. The present high resolution images show that there are  $T_c$  anomalies at several of the shocks known to exist in this field of view (but certainly not in all the known shocks). The anomalous  $T_c$  feature to the southwest from HH 202-S corresponds to a faint shock visible only in H $\alpha$  and [O III], but not in [N II] (O97).

The Paranal spectra described in § 3.5 were centered on HH 202-S. The spectra show no 4686 Å emission. However, there is a considerable enhancement of [Fe III] emission. In a sample centered on HH 202-S, the flux ratio of 4658 Å to H $\beta$  was 0.031, which predicts a 4702 to H $\beta$  ratio of 0.010 (using the flux ratio from EPTE98). Together with a normal 4713 contribution, this would raise the ratio  $N_{\text{OBS}} / N_{\text{CONT}}$  to 1.18, which would artificially reduce the 4363 ratio by a factor of 4.6, and decrease the derived value of  $T_c$  to 6300 K. Since the

Paranal sample on HH 202-S was 20'' long and the object is much smaller, the contamination would be much larger on the object itself and the artificially derived  $T_c$  correspondingly lower. Direct confirmation of contamination by 4702 was obtained by high velocity resolution spectra obtained by co-author O'Dell and Will Henney with the Manchester Echelle Spectrometer (Meaburn, et al. 1984) on the 2.1-m telescope at San Pedro Martir observatory on 2002 October 23, where one sees significant enhancement of that line, peaking at the optically brightest portion of HH 202-S, with no indication of 4686 Å emission.

This means that enhanced [Fe III] emission is a common feature of the anomalously low  $T_c$  spots seen in Figure 2, rendering useless the  $T_c$  values there. Why [Fe III] is enhanced in these shocks is in itself an interesting problem that should be addressed.

### 4.3. Spurious “High $T_c$ ” values in this study

Several proplyds occur within our sample, the brightest within CCD2-4 are 141-301 and 182-413. These proplyds and the fainter, less well resolved ones all show enhanced values of  $T_c$ . In this case the anomaly is probably due to the mis-application of equation (5), which is applicable only in the limit of electron densities ( $N_e$ ) low as compared with the critical density ( $N_{crit}$ ) for [O III].  $N_{crit}$  is the density at which collisional de-excitation of the upper state giving rise to an emission line is equal in probability to a spontaneous emission. This is only of concern for the 5007 Å line as its  $N_{crit}$  value is much lower than that for the 4363 Å line. Rubin et al. (2003, henceforth R2003) give  $N_{crit}(5007 \text{ Å}) \simeq 6.4 \times 10^5 \text{ cm}^{-3}$ , which is much higher than densities encountered in the nebula, but comparable to characteristic values for the proplyds (O'Dell 1998a). This means that in the local ionization fronts of the proplyds the 5007 Å emission is being suppressed by collisional de-excitation and the  $T_c$  value derived from equation (5) will be an upper limit. This same interpretation is applied by R2003 to their high [O III]  $T_c$  for the proplyd 159-350, which lies in the center of our CCD1 image and fell in their long slit spectrum. In their models of the proplyds close to  $\theta^1$  Ori C Henney et al. (2002) argue that the formal temperatures derived without consideration of collisional de-excitation would be about 20,000 K. If the densities of the more distant proplyds are much lower, as indicated by their surface brightnesses, then the effects of collisional de-excitation are less and some of the temperature increase we find is real.

It is not clear if the similar local increase in  $T_c$  at the jet feature just south of the dark rim (O'Dell & Yusef-Zadeh 2000) in the southeast corner of CCD4 is due to this same effect. The jet has a known high radial velocity (O'Dell et al. 1997) and proper motion (O'Dell & Doi 2003), so it may be that  $T_c$  is enhanced where this flow shocks against ambient nebular

gas.

#### 4.4. Small Scale Variations in $T_c$

Figure 2 indicates that there are variations in  $T_c$  even though we've shown in § 4.1 that these variations are not a function of distance from  $\theta^1$  Ori C.

The smaller scale changes have been illuminated by looking at the three sample regions depicted in Figure 2, these samples being selected to be free of the [Fe III] contamination. The results are shown in Figure 3. In each case the range of temperature is  $\pm 1000$  K. For reference, random noise at the level of 5.7 % probable error is shown, this being the level expected for the bright portions. The southwest sample is about one fourth the surface brightness of the other samples. The noise level was brought down to that of the other samples by taking samples of 2x2 pixels in this region. Examination of Figure 3 shows that the face of the nebula is mottled with small scale variations of  $T_c$  with angular dimensions of about  $10''$  and amplitudes of about 400 K.

#### 4.5. Fourier Analysis of two regions of the $T_c$ image

In order to gain a more quantitative evaluation of the data, we performed a Fourier analysis of two regions of the  $T_4$  image. The first was a 400x400 pixel section in the northwest portion of CCD2 and the second was 250x250 pixels in the northeast section of CCD4, both being free of camera scars and the local apparent  $T_c$  drops that are due to shocks, as discussed in § 4.2. The analysis was done using STSDAS tasks with IRAF. The procedure was the same for each sample. The first step was to subtract the average value of the sample from each pixel and then to make a power spectrum of the resulting image, using the task *powerspec*. A radial profile was taken of the power spectrum image using the center as the origin. The result was a profile that dropped down to a constant value at large spatial frequency values and represents the noise level due to the Poisson noise in the data. This constant value was then subtracted from the radial profile of the power spectrum. The resulting noise-subtracted power spectrum was then converted to the physically more meaningful length space by multiplying the power spectrum in spatial frequency by the square of the frequency and binning the result in the spatial dimension. The results are shown in Figure 4 and Figure 5. These plots show that there is a large amount of power at the finest scales (sub-arcsec) but that power is found at all scales. This analysis is similar to that of Vannier et al. (2001) of H<sub>2</sub> emission arising near the imbedded BN-KL sources to the north of CCD4.

## 5. Values of $t_A^2(\text{O}^{++})$ and estimates of $t^2(\text{O}^{++})$ and $t^2(\text{H}^+)$

The aims of this section are to estimate representative values of the temperature variations [ $t^2(\text{O}^{++})$ ,  $t^2(\text{O}^+)$ , and  $t^2(\text{H}^+)$ ] in the Orion Nebula in order to compare them with predictions of photoionization models and to be able to study the physical conditions of the nebula including its chemical composition. We proceed in three steps: 1.) use of the  $T_c$  map obtained in this paper to determine  $t_A^2(\text{O}^{++})$  across the plane of the sky (this is the first detailed 2-dimensional set of temperatures across of the Orion Nebula), 2.) estimate the 3-dimensional value of  $t^2(\text{O}^{++})$ ; 3.) estimate  $t^2(\text{H}^+)$  including both the  $\text{O}^+$  and the  $\text{O}^{++}$  regions.

### 5.1. Values of $t_A^2(\text{O}^{++})$ measured in the plane of the sky

In order to obtain the observed mean square temperature variation in the plane of the sky,  $t_A^2(\text{O}^{++})$ , we will define a set of equations. The average temperature,  $T_0(X^{+i})$ , and the mean square temperature fluctuation,  $t^2(X^{+i})$ , are given by

$$T_0(X^{+i}) = \frac{\int T_e(\mathbf{r})N_e(\mathbf{r})N(X^{+i};\mathbf{r})dV}{\int N_e(\mathbf{r})N(X^{+i};\mathbf{r})dV}, \quad (9)$$

and

$$t^2(X^{+i}) = \frac{\int (T_e - T_0(X^{+i}))^2 N_e N(X^{+i}) dV}{T_0^2 \int N_e N(X^{+i}) dV}, \quad (10)$$

respectively, where  $T_e$  and  $N_e$  are the local electron temperature and density,  $N(X^{+i})$  is the local ion density corresponding to the observed emission line, and  $V$  is the observed volume (Peimbert 1967). By recognizing that the observations correspond to averages over a given line of sight, it becomes necessary to define the columnar temperature,  $T_c$ , as

$$T_c(X^{+i}; \alpha, \delta) = \frac{\int T_e N_e N(X^{+i}) dl}{\int N_e N(X^{+i}) dl}, \quad (11)$$

where  $\alpha$  is the right ascension and  $\delta$  is the declination of a given line of sight (corresponding to a given pixel). Then, the average temperature can be written as

$$T_0(X^{+i}) = \frac{\int T_c(X^{+i}; \alpha, \delta) \int N_e N(X^{+i}) dl dA}{\int \int N_e N(X^{+i}) dl dA}, \quad (12)$$

and the mean square temperature variation over the plane of the sky,  $t_A^2$ , can be defined as:

$$t_A^2(X^{+i}) = \frac{\int (T_c(X^{+i}) - T_0(X^{+i}))^2 \int N_e N(X^{+i}) dl dA}{T_0(X^{+i})^2 \int \int N_e N(X^{+i}) dl dA}. \quad (13)$$

In Table 2 we list a set of  $t_A^2(\text{O}^{++})$  values obtained from equation (13) and from the  $T_c(\alpha, \delta)$  map presented in Figure 2. To determine  $t_A^2(\text{O}^{++})$  we have excluded several features in order to diminish the noise of the samples: the pixels with very low flux, where we expect the temperature deviations to be mostly due to errors and not to physical inhomogeneities; the shocks, where the destruction of dust could be enhancing the [Fe III] 4702 line and thus producing spurious temperatures; the proplyds, whose density is not well represented by equation (5); the seams between the CCDs, where there are border effects. Keeping in mind these exclusions we defined the six regions from Table 2 as follows: regions 1 and 2 include most of the pixels of the SE and SW regions as defined in Figure 3; region 3 includes most of the pixels in a  $54'' \times 73''$  region in the eastern part of CCD4; region 4 is the largest sample, it includes most of the pixels from CCD2, CCD3, and CCD4; finally region 5 includes approximately 72% of the pixels of region 4 where, in order to enhance the S/N ratio, the southern 10% of CCD2, the southwestern 50% of CCD3, and the western 25% of CCD4 have been removed, the regions removed are the ones of relatively low emission measure. Although the signal in CCD1 was high, the presence of scattered light artifacts (c.f. § 2) prevents its use in our analysis.

Column 2, of Table 2, presents the number of independent temperatures used in the region; column 3 presents the average temperature, weighted by  $\int N(\text{O}^{++}) \times N_e dl$  (defined in equation (12) ) ; while column 4 presents the measured  $t_A^2(\text{O}^{++})$  for each region.

The  $t_A^2$  of regions 1, 2, and 3 is in the 0.005–0.016 range. The differences in  $t_A^2$  are real since they are larger than the expected observational errors. This could have 2 explanations: a) region 3 is more homogeneous than regions 1 and 2; b) another possibility is that  $t^2$  is similar in the 3 regions, and the variations along each line of sight in region 3 are larger, while there are not so many variations along the lines of sight in regions 1 and 2, thus giving a set of more homogeneous values of  $T_c$  for region 3 than for regions 1 and 2.

We added most of the pixels from CCD2, CCD3, and CCD4 to generate region 4. Figure 6 presents a histogram of the 1.5 million temperatures included in region 4. The mean square temperature deviation obtained from the histogram is  $\sigma(T)^2/T^2 = 0.018$ ; which is not  $t_A^2$ . It is not possible to derive directly  $t_A^2$  from the histogram since each temperature has to be weighted by the corresponding emission measure (see equation (13)). After weighting each  $T_c$  value for the emission measure we obtain a  $t_A^2(\text{O}^{++}) = 0.0096$  for region 4.

We still have to subtract a value associated with the noise. The average p.e. in  $T_c(\text{O}^{++})$  for the whole sample is 5.7 %, however this value is for an average pixel, while the measured  $t_A^2(\text{O}^{++})$  gives more weight to the brightest pixels, the ones with the smaller errors. By considering that the average pixel is 1.89 times fainter than the average pixel weighted by emission measure, we expect the representative p.e. to be 4.2 %, which corresponds to an



error on  $t_A^2$  of 0.0017, that is a  $t_A^2(\text{O}^{++}) = 0.0079$ .

If we take out the noisiest parts of region 4 (the outermost parts), we have region 5. Here the measured  $t_A^2(\text{O}^{++}) = 0.0084$ . For region 5 we expect the noise to be about 2/3 the noise of the entire region, that is a p.e. of 3.8 % per pixel. In region 5 the average pixel is 1.31 times fainter than the average pixel weighted by emission measure; thus we expect the representative p.e. to be 3.3%, which corresponds to an error on  $t_A^2$  of 0.0011, that is a  $t_A^2(\text{O}^{++}) = 0.0073$ .

We expect the  $t_A^2$  result for region 5 to be more accurate; however, by excluding the outermost parts we seem to be ignoring a fraction of the object which is intrinsically cooler. Therefore we will adopt the value derived from region 4,  $t_A^2(\text{O}^{++}) = 0.0079$ , as representative for the whole object.

This value is similar to the one obtained by R2003 where they find  $t_A^2$  values of 0.0095, for their slit 1, and 0.0104, for their slit 2. Unfortunately, their slits 1 and 2 are located in our unusable CCD1, which precludes a direct comparison.

## 5.2. Relation of $t_A^2(\text{O}^{++})$ measured in the plane of the sky to its 3-dimensional value, $t^2(\text{O}^{++})$

Up to this point we have presented the results in terms of  $t_A^2(\text{O}^{++})$ , but what is of physical interest are the variations in three dimensions  $t^2(X^{+i})$ . In order to obtain the total  $t^2(X^{+i})$  value we need to consider the variations along the line of sight. It can be shown that the relevant equation is:

$$t^2(X^{+i}) = t_A^2(X^{+i}) + \langle t_c^2(X^{+i}; \alpha, \delta) \rangle, \quad (14)$$

where  $t_c^2$ , the variation along a given line of sight, is given by:

$$t_c^2(X^{+i}; \alpha, \delta) = \frac{\int N_e N(X^{+i})(T_e - T_c)^2 dl}{T_c^2 \int N_e N(X^{+i}) dl}, \quad (15)$$

and the average over all lines of sight is given by:

$$\langle t_c^2(X^{+i}; \alpha, \delta) \rangle = \frac{\int t_c^2 T_c^2 \int N_e N(X^{+i}) dl dA}{T_0^2 \int \int N_e N(X^{+i}) dl dA}. \quad (16)$$

There are two estimates that we can make of  $t_c^2$ : the first based on geometrical considerations and the information contained in  $t_A^2(X^{+i})$ ; and the second based on the ratio of  $X^{+i}$  collisionally excited lines to  $X^{+i-1}$  recombination lines.

From geometrical considerations one would expect the inhomogeneities of one additional dimension,  $t_c^2$ , to be at least half as large as the inhomogeneities of two dimensions,  $t_A^2$ ; this works for large scale inhomogeneities. The power included in  $t_c^2$  increases in the presence of small scale inhomogeneities. This is because the many independent thermal elements along each line of sight will be masked in the averaging process, greatly reducing the total  $t_A^2$  compared to  $t^2$ . Therefore,  $t_c^2$  would be expected to be much larger than  $t_A^2$ . From the previous considerations, we estimate that  $0.5 \lesssim t_c^2/t_A^2 \lesssim 2.0$ ; this result is very model dependent which is reflected by the large range in the estimated  $t_c^2/t_A^2$  value. This estimate together with the  $t_A^2(\text{O}^{++})$  value derived in the previous subsection yield  $0.004 \lesssim t_c^2(\text{O}^{++}) \lesssim 0.016$ .

From the ratio of O II recombination lines to [O III] lines in two regions of the Orion Nebula EPTE98 find that  $t^2(\text{O}^{++}) = 0.023 \pm 0.005$ . This  $t^2$  value is representative of a very small fraction of the nebula, so we expect it to be a lower bound to the total  $t^2(\text{O}^{++})$ . At the same time it must be bigger than  $t_c^2(\text{O}^{++})$  because it represents an average over more than one line of sight. This argument, together with the  $t_A^2(\text{O}^{++})$  value estimated in the previous subsection, yields  $0.010 \lesssim t_c^2(\text{O}^{++}) \lesssim 0.028$ .

By combining both estimates we find  $t_c^2 = 0.013 \pm 0.005$ , which implies that there is power in small scale inhomogeneities. Our preferred value of  $t_c^2$  together with the  $t_A^2$  measured in the previous subsection and equation (14) gives us a  $t^2(\text{O}^{++}) = 0.021 \pm 0.005$  value.

### 5.3. An estimate of the temperature variations for the whole H II region

We are interested in the global  $t^2$  value that we will define as:

$$t^2(\text{H II}) = t^2(\text{H}^+) \quad (17)$$

in order to derive the physical conditions in the H II region.

In an H II region, like the Orion Nebula, where oxygen is only once or twice ionized, it is useful to define a value  $\gamma$ , that characterizes the degree of oxygen ionization, as:

$$\gamma = \frac{\int N_e N(\text{O}^{++}) dldA}{\int [N_e N(\text{O}^+) + N_e N(\text{O}^{++})] dldA}; \quad (18)$$

for such an H II region  $t^2(\text{H II})$  is given by (Peimbert, Peimbert, & Luridiana 2002):

$$t^2(\text{H II}) = \gamma t^2(\text{O}^{++}) \frac{T_0(\text{O}^{++})^2}{T_0(\text{H}^+)^2} + (1 - \gamma) t^2(\text{O}^+) \frac{T_0(\text{O}^+)^2}{T_0(\text{H}^+)^2} + \gamma(1 - \gamma) \frac{[T_0(\text{O}^+) - T_0(\text{O}^{++})]^2}{T_0(\text{H}^+)^2}, \quad (19)$$

the first term corresponding to the temperature variations in the  $O^{++}$  zone, the second term corresponds to the variations in the  $O^+$  zone, and the third term corresponds to the thermal variations introduced by having two zones with different average temperatures.

From the observations of Peimbert & Torres-Peimbert (1977) and EPTE98 it follows that  $\gamma$  decreases from about 0.85 near the center of the nebula to about 0.15 in the outer regions. We will adopt a value of  $\gamma = 0.6$  as representative of the whole object.

It is necessary to estimate  $t^2(O^+)$ . Since  $T(O^+)$  is rarely measured we will use  $T(N^+)$  as a surrogate since we expect both temperatures to be similar as they arise from the same narrow  $H^+ + He^o$  zone. R2003 present values of  $t_A^2(N^+)$ ; their measured values are in very good agreement with their measured values of  $t_A^2(O^{++})$ ; therefore we will assume  $t_A^2(O^+) = t_A^2(O^{++})$ . It is impossible, however, to estimate  $t_c^2(O^+)$  from any set of observations available. From the geometrical arguments presented in the previous section and the similarities between the  $t_A^2(O^{++})$  and  $t_A^2(O^+)$  presented by R2003 we will assume also that  $t_c^2(O^+) = t_c^2(O^{++})$ , and consequently that  $t^2(O^+) = t^2(O^{++})$ .

To compute the final term in equation (19) we need to estimate the differences in temperatures between the  $O^+$  and  $O^{++}$  zones (again we will use  $T(N^+)$  as a surrogate). Our observations do not yield  $T(N^+)$  values, therefore we are forced to look for them in the literature. We are more interested in finding  $T(N^+) - T(O^{++})$  than  $T(N^+)$  to avoid possible biases, since the calibration is uncertain by a few hundred degrees (see final paragraphs of sections 3.1 and 3.5); an additional advantage of such comparison is that papers in the literature cover regions considerably smaller than the one presented in this paper. EPTE98 have measured  $T(N^+) = 10200$  K and  $T(O^{++}) = 8300$  K; while R2003, for their slits 1 and 2 and assuming  $N_e = 5000 \text{ cm}^{-3}$ , obtain  $T(N^+) = 10050$  K and  $T(O^{++}) = 8200$  K. By averaging the innermost 9 regions of B91, we find  $T(N^+) = 10200$  K and  $T(O^{++}) = 9050$  K. These three results give us an average  $T(N^+) - T(O^{++}) = 1650$  K. As mentioned before, we have adopted a  $\gamma = 0.6$ , giving a  $T_0(H^+)$  approximately 700 K higher than  $T(O^{++})$ .

The inputs presented above yield values of 0.011, 0.010, and 0.007 for the three terms in equation (19). Therefore the total magnitude of the temperature fluctuations becomes  $t^2(H\text{ II}) = 0.028 \pm 0.006$ . Notice that for values of  $\gamma$  in the 0.3 to 0.7 range the change in total  $t^2$  is very small since  $t^2(O^+) = t^2(O^{++})$ , thus changes in  $\gamma$  will make very small changes in the sum of the first 2 terms of equation (19), while the third term will change by less than 15% for that range of  $\gamma$ .

The total  $t^2(H\text{ II})$  value derived in this paper is considerably larger than the 0.004 value derived by Peimbert et al. (1993) from the one dimensional model of the Orion Nebula presented by B91.

## 6. Comparison with previous work

The type of temperature variations reported here have not been seen before because previous slit spectra determinations usually employed integrations over long areas of the nebula. The best slit spectrum sub-sampling until R2003 is in B91, where the sample sizes were as short as  $16''$  and one could see sample to sample changes in  $T_c$  of about 300 K (B91, Table 5). Their changes were comparable to the uncertainties in their derivations of  $T_c$  from the [O III] line ratios, so this variation did not attract attention. However, the B91 variations are consistent with the small scale variations we see in our Figure 3.

A much more valuable study is that of R2003, where they employed the HST's STIS (Space Telescope Imaging Spectrometer) in a long slit mode to determine  $T_c$  in samples of  $0.5'' \times 0.5''$  in both [O III] and [N II]. They presented results for about 400 samples from each of four slit settings, two within our CCD1 field and the others near or off the southeast corner of our CCD2 field. It is possible to use this data to estimate a lower limit to  $t^2(\text{H II})$  using the same procedure as in the previous section.

From their slits 1 and 2, those included in our map, it is found that  $T_0(\text{O}^{++}) = 8200$  K and  $T_0(\text{N}^+) = 10050$  K; notice that these  $T_0$ 's corresponds to two rectangular columns of the nebula and not to a large volume. From these slits we also find  $t_A^2(\text{O}^{++}) = 0.010$  and  $t_A^2(\text{N}^+) = 0.009$ .

From R2003 observations it is not possible to obtain direct estimates of the  $\text{O}^{++}$  and  $\text{N}^+$  temperature fluctuations along any given line of sight; so we will use  $t_A^2(\text{O}^{++})$  and  $t_A^2(\text{N}^+)$  as lower bounds to  $t^2(\text{O}^{++})$  and  $t^2(\text{N}^+)$ .

To estimate the two zone temperature term, the term due to the difference between  $T_0(\text{O}^{++})$  and  $T_0(\text{N}^+)$  (see equation (19) , we will adopt  $\gamma = 0.7$ . This, together with  $T_0(\text{O}^{++})$  and  $T_0(\text{N}^+)$ , yields a contribution of 0.009.

Finally, adding these 3 terms, we obtain  $t^2(\text{H II}) \geq 0.019$ . This lower limit to  $t^2(\text{H II})$  is consistent with our determination and with the  $t^2$  determination by EPTE98. Moreover it is already a factor of 5 higher than the values predicted by one-dimensional photoionization models of the Orion Nebula, like the one by B91.

## 7. Discussion

In this section we will review the large scale structure of the Orion Nebula (§ 7.1), present a conundrum arising from the presence of fine scale structure in images (§ 7.2), demonstrate that high resolution spectra and line ratio changes argue for a three dimensional fine scale

structure (§ 7.3), argue that the ionization front is advancing into a highly clumpy PDR (§ 7.4), show how these clumps can lead to low  $T_e$  shadows within the ionized layer that can help to explain the  $t^2$  phenomenon in the region of low ionization regions (§ 7.5), and present a preliminary discussion of the effect of these clumps on the anomalous line-broadening in Orion (§ 7.6).

### 7.1. The global structure of the Orion Nebula

The accepted model for the Orion Nebula is that of a blister. The visible nebula is the result of a thin layer of photoionized gas on the front of a giant molecular cloud, with a dense photon-dominated region (PDR) (van der Werf et al. 1996), also known (Young Owl et al. 2000) as a photodissociation region, on the neutral side of the ionization front. Gas is accelerated away from this ionization. The dominant ionizing star is  $\theta^1$  Ori C which lies at about 0.25 pc in front of the ionization front. In the foreground is an irregular veil of neutral material that produces most of the extinction (O’Dell 2002). This model is reviewed in detail in a recent review article (O’Dell 2001b, henceforth OD2001. The basic physics is discussed in a review paper by Ferland (2001).

The shape of the ionization front has been derived (Wen & O’Dell 1995, henceforth WO95) using a basic process originally proposed by Gary Ferland in B91. This draws on the fact that at a substellar point, the surface brightness in a recombination line (for example  $H\alpha$ ) is directly proportional to the local flux of ionizing photons. WO95 solved the more general problem, where the line of sight to a point in the nebula does not pass through the ionizing star. They showed that the ionization front is an irregular concave form, with an escarpment that explains the Bright Bar feature running near  $\theta^2$  Ori A and has a dominant hill to the southwest of  $\theta^1$  Ori C, where the Orion-S radio and infrared sources are located. O’Dell & Doi (2003) have shown that the latter region is the source of multiple optical and radio outflows and probably contains a secondary source of star formation. This model was derived using a resolution of  $2''$ . Because of the progressive nature of the calculation of the shape of the surface, it is most accurate near the direction of  $\theta^1$  Ori C.

The only diagnostics that we have along the line of sight into the nebula are the increasingly blue-shifted emission from the higher ionization states that are found further from the MIF and forbidden line doublet intensities that indicate a decreasing density with increasing distance from the MIF (OD2001). These few tests that we have are consistent with the model.

A detailed hydrodynamic model of the Orion Nebula has not been calculated, however,

it is expected that the high density in the PDR region is the result of a shock moving into the molecular cloud and that the ionization front is slowly progressing into the neutral region.

## 7.2. A quandary presented by the appearance of fine scale structure in the Orion Nebula

The HST images of the Orion Nebula are filled with detail, especially in the inner regions. At first blush, this appears to present a fundamental quandary if the standard model for the nebula is correct. One can derive a formal thickness ( $L$ ) for the ionized layer, using the assumption that the density is constant and knowing the emissivity in the recombination line being observed. WO95 show that this value is characteristically about 0.13 pc for the central part of the nebula, which corresponds to an angle of  $58''$  if the distance to the nebula is 460 pc (Bally, O'Dell, & McCaughrean 2000). They also show that if the density has an exponential decrease, its scale-height will be  $L/2$  ( $29''$ ) and the emissivity would decrease with a scale-height of  $L/4$  ( $15''$ ). This means that in the standard model one should not be able to see variations in the structure of the nebula with size scales smaller than about  $15''$ .

One certainly see lots of fine-scale (less than  $15''$ ) structure in ground-based and HST images. Some of this can be attributed to variations in the amount of extinction (O'Dell & Yusef-Zadeh 2000), most of which is caused by the foreground neutral veil of material (OD2001). However, the extinction corrected images in  $H\alpha$  show significant structure right down to the limit of the extinction corrections, which was about  $1.7''$ . This is shown in Figure 7, which is a profile of the extinction corrected  $H\alpha$  image of the nebula (O'Dell & Yusef-Zadeh 2000) derived with a resolution of  $1.7''$  and taken across the velocity sample region designated in Figure 1.

There are even smaller features, which appear to be a continuation of the structure, as shown in the HST images, while the smallest features are due to the outflows from young stellar objects and the shocks they create in the low density ambient gas (O'Dell & Doi 2003, OD2001) and are seen in the HST images to be sub-arcsecond in extent.

The presence of fine scale structure associated with the main emitting layer of ionized gas presents a fundamental challenge to the accepted model of the nebula. The structure is there, for we see it, but if the ionized gas was simply a smooth flow of gas away from a homogeneous ionization front, we should not see any small scale structure. We demonstrate in § 7.5 and § 7.6, that the resolution of the quandary lies in the emitting layer having a much more complex structure than assumed in published models.

### 7.3. Substructure in the main emitting layer revealed by fine scale velocity variations and line ratios

There are two additional lines of evidence indicating that small scale structure exists within the ionized layer, these being the structure seen in the velocities and fine scale variations in the ionization. Both argue for structure down to at least a few arcseconds.

The internal velocities within the Orion Nebula have been the subject of investigation for nearly a century, beginning with a Fabry-Perot study by Fabry (Buisson, Fabry, & Bourget 1914), an extensive mapping using photographic detectors (Wilson et al. 1959), and a series of studies in various emission lines using CCD detectors ([O III], Castañeda 1988; [O II], Jones 1992; [O I], O’Dell & Wen 1992; [S III], Wen & O’Dell, 1993) at the Kitt Peak National Observatory Coudé Feed spectrograph at selected position angles with respect to the Trapezium stars. This work was used to compare the radial velocities with the predictions of turbulence within a thin ionized layer (von Hörner 1951) and the results are summarized in OD2001. A more ambitious and complete mapping of the radial velocities is now being created as part of the Rice University PhD thesis of Takao Doi, who is creating velocity images of the Huygens region at resolutions of  $10 \text{ km s}^{-1}$  and  $2''$  in the  $\text{H}\alpha$ , [O III]  $5007 \text{ \AA}$ , and [N II]  $6583 \text{ \AA}$  lines, and a similar study at the Instituto de Astronomía, UNAM, Morelia, México in the red [S II] doublet lines by W. J. Henney & M. T. García-Díaz that uses in part data obtained by co-author O’Dell.

With the permission of our colleagues we have used their north-south orientation slits to create Figure 8 and Figure 9. These are spectra taken from the velocity sample region indicated in Figure 1 and used for the creation of the surface brightness profiles of Figure 7. The instrumental full width at half maximum intensity (FWHM) was very close to  $10 \text{ km s}^{-1}$  in each case. Although the original samples along the slit were at intervals of  $0.64''$ , the seeing was characteristically about  $2''$  during the observations. The former figure shows a half tone depiction of the spectra in lines characterizing various parts of the ionized layer and the latter presents contour diagrams of the same data.

The power of this approach lies in the fact that various emission lines are characteristic of different samples of the ionized layer. Although this fact is implicit in the discussion of several texts, perhaps the best illustration is in a discussion of structure of the Helix Nebula (O’Dell 1998b).  $\text{H}\alpha$  emission comes from throughout the ionized layer, its emissivity being weighted towards the lower  $T_e$  regions along the line of sight. The forbidden line emissivity in [S II], [N II], and [O III] are all weighted towards the higher  $T_e$  regions along the same line of sight. Delineation of information about structure along the line of sight is also provided by the ionization differences. [S II] emission will arise exactly in the ionization front, where ionization of hydrogen rapidly transitions from nearly unity to nearly zero. A good fraction

of the [N II] emission will occur in the adjacent thin  $H^+ + He^0$  zone, while the [O III] emission will arise in the outermost (closest to the observer)  $H^+ + He^+$  zone.

We see in Figure 8 and Figure 9 that there is considerable velocity variation along the slit and that the velocity in one ion is not well correlated with that in the other ions. Thermal broadening of the  $H\alpha$  line precludes a detailed analysis of its velocity structure, but is low enough in the other, more massive, ions to see the differences clearly. One sees that the narrower the expected emitting region, the more structure there is along the slit. [S II] emission gives evidence for velocity structure with a scale of the seeing values of  $2''$  and [O III] emission has a characteristic size scale down to about  $5''$ . These data argue that structure exists within the main ionized layer at sizes down to at least  $2''$  and that gas of different states of ionization is moving at different velocities. It is the spatially unresolved average velocity along the slits which give the characteristic progression to more blueshifted radial velocities at higher states of ionization that is the earmark of a thin blister of gas expanding towards the observer.

The second line of evidence for fine scale structure within the nebula is from comparison of emission from very different states of ionization or conditions of emissivity. For this comparison we used two pairs of images, whose closeness in wavelength essentially eliminate the effects of interstellar extinction. The first pair used the F487N images, which are primarily due to  $H\beta$  emission whose emissivity is like that of  $H\alpha$  in that it selectively comes from the lower  $T_e$  regions, and the F502N images, which are primarily emission from [O III] 5007 Å high  $T_e$  collisionally excited regions. The second pair used the F656N  $H\alpha$  filter and the [N II] F658N filter. The considerations for the emissivity are similar in the second pair of filters, but the emitting layer of the [N II] emission should be thinner. The hydrogen emission arises from throughout the ionized zone, but the [N II] and [O III] emission arise from selected zones, as described earlier in this section.

The results of these comparisons are shown pictorially in Figure 10. One sees that there are wide variations in these ratios. Some of these changes are due to shocks caused by outflows from pre-main sequence stars (O'Dell & Doi 2003) while others such as the Bright Bar region in the southwest corner of the images is due to large scale topographic features of the ionization front (O'Dell & Yusef-Zadeh 2000). In addition to these, there are many additional features. A more quantitative depiction is shown in Figure 11 and Figure 12, where profiles along the same region as the velocity samples are presented. We see fine scale structure in the ratios down to nearly the size of the  $1'' \times 2''$  bins over which the data was averaged, although a characteristic value would be  $3''$  to  $4''$ . The probable errors of the ratios were derived from the total counts used in their calculation and are 1.8 % for the F658N/F656N ratio and 1.2 % for the F502N/F487N ratio. As expected, the peaks



are sharper in the F658N/F656N ratio, indicating that the sources are small concentrated regions. The fact that there is a general anti-correlation of the ratios indicates that the variations are largely due to ionization structure, rather than temperature differences.

In summary, we can say that both the spatially resolved high resolution velocity data and the line ratio data indicate structure in the main ionized layer of 3'' to 5''.

A comparison with a profile of the results of the determination of  $T_c$  is also useful and is shown in Figure 13, where a profile along the same region as the velocity data is shown. We see that the proplyd 141-301 shows the common characteristic of the other proplyds, in having a higher than normal formal value of  $T_4$ , but, as shown in § 4.3, this is probably due to collisional de-excitation of the electron state giving rise to the 5007 Å emission. The “JET” feature shows a similar enhancement, which may also be due to having densities comparable to the critical density for this nebular transition, but it could be real, being the result of shock heating at the interface with the ambient nebular gas. Aside from these features, there are variations in  $T_c$  all along the slit. In the well exposed region from 50'' to 150'' we calculate that the probable error of  $T_c$  is 0.5% i.e. 45 K., which is small as compared with the observed variations. There are no obvious general patterns of changes with the extinction corrected surface brightness in  $H\alpha$ , the velocity changes, nor the line ratios.

#### 7.4. The effects of the ionization front advancing into a clumpy PDR

There is considerable evidence that the PDR behind the ionization front of the Orion Nebula is very clumpy (Tauber, Goldsmith, & Dickman 1991, Hogerheijde, Jansen, & van Dishoeck 1995). HCN and HCO<sup>+</sup> observations by Young Owl et al. (2000) demand that the portion of the PDR seen obliquely behind the Bright Bar feature possesses dense clumps ( $3 \times 10^6 \text{ cm}^{-3}$ ) embedded within an interclump medium of lower density ( $5 \times 10^4 \text{ cm}^{-3}$ ). More direct observations come from imaging in H<sub>2</sub>. van der Werf et al. (1996) show that clumps exist from a scale of 40'' down to their resolution limit of 1.5''. The highest angular resolution study in H<sub>2</sub> is that of Vannier et al. (2001) who studied a region northwest of  $\theta^1$  Ori C at a resolution of 0.15''. Again, they saw clumpy structure, in this case going down to 1.5''-2.0''. A clumpy structure in the PDR is not unexpected and there would be several instability mechanisms that operate there (Capriotti 1973, Brand 1981, Vishniac 1994, García-Segura & Franco 1996, Williams 1999).

The implications of these clumps for the nature of the ionized layer of gas in the nebula are very important since it is into these clumps and the interclump medium that the ionization front advances. Where the density is lower, the advance will be more rapid. The

expected rate of advance of the ionization front is not known as the hydrodynamic problem has not been solved. The Orion Nebula is old enough that it is in a state of quasi-equilibrium and the velocity will depend on many factors, including whether or not the photoionizing star  $\theta^1$  Ori C has a velocity component towards or away from the molecular cloud.

This means that one would expect the ionization front advancing into a clumpy PDR to move beyond the dense clumps and be retarded at the clumps, so that a microscopic view of the ionization front would be like that of a stubble-field. The region behind a dense knot would then be shadowed from ionizing Lyman Continuum (LyC) radiation coming directly from  $\theta^1$  Ori C and would be illuminated only by diffuse (sometimes called scattered) LyC photons. Where the density is insufficient to form a quasi-static ionization front, the clumps will simply retard the advance of the ionization front, while the dense clumps will form a small local ionization front that will exist until it has lost sufficient material through photoevaporation that the ionization front can penetrate, then totally disperse it.

### **7.5. Low $T_e$ regions behind clumps within the ionized gas of the ionized layer of gas**

The shadowed regions behind the knots within the ionized layer can be sources of low temperature emission and of temperature variations, therefore they will increase the  $t^2$  value. The photoionization equilibrium in such a shadowed region was considered 30 years ago (Van Blerkom & Arny 1972, Kirkpatrick, 1972, Capriotti 1973), but it is only recently that the more general case has been considered (Cantó et al. 1998, henceforth C98). The region illuminated only by diffuse LyC will see a lower temperature radiation field because most of the recombinations of  $H^+$  that produce the diffuse LyC will result in a photon just above the ionization threshold, while the direct stellar field will have more high energy photons and produce higher  $T_e$  regions. C98 have solved the general problem, rather than trying to apply their calculations to only a specific object, including the role of ambient gas density and the time variability of the shadowed zone structure. When the combination of the stellar radiation density (the diffuse radiation field density is about 15 % of that) and gas density is right an ionization front can form immediately at the edge of the shadowed cylinder of gas. As the radiation density increases and/or the density decreases, the ionization front can form within the shadowed cylinder and even produce a condition where the shadowed cylinder is completely photoionized. C98 argue that  $T_e$  within the ionized shadow zone will be about 6000 K, considerably cooler than that of the directly illuminated gas.

The radiation from the shadowed zone can be seen by the distant observer for two reasons. In some cases the angle between the line of sight from the observer to  $\theta^1$  Ori C can

be quite different from the angle between  $\theta^1$  Ori C and a local spot on the ionization front, allowing direct view of the shadowed region. Even when that is not the case, a significant fraction of the radiation from the shadowed region will be scattered by dust in the nearby PDR, in the same way that radiation from the ionized layer is scattered and produces the observed redward asymmetry of the emission lines (O’Dell, Walter, & Dufour 1992 , Henney 1998).

### 7.5.1. Proplyds

Shadowed regions have already been detected in the Orion Nebula. In a study of both the Cometary Knots in the Helix Nebula and the proplyds in the Orion Nebula, O’Dell (2000) showed that the proplyds cast ionization shadows as long as 0.2 pc. The proplyds are optically thick to LyC radiation (O’Dell 1998a) and in that sense resemble the optically thick clumps we argue exist at the main ionization front of the nebula. The proplyd ionization shadows are most visible when the geometry is such that the shadow falls into the ionized layer that provides most of the radiation identified as the nebula. O’Dell (1998a) showed that the shadows of the proplyds covered about 0.5% of the view from  $\theta^1$  Ori C. By assuming: pressure equilibrium,  $1 - \gamma = 0.4$ ,  $T(\text{N}^+) = 10,100$  K (B91, EPTE98, R2003) for the directly illuminated regions, and  $T(\text{N}^+) = 6,000$  K (C98) for the shadowed regions we obtain a contribution of 0.0093 to  $t^2(\text{O}^+)$  (see equation (10)), that is a contribution of 0.0043 to the total  $t^2$  (due to second term of equation (19)) . To reach the estimated 0.011 contribution to  $t^2$  due to the  $\text{O}^+$  zone, we need an additional 0.7% of the volume of the nebula to be in a different type of ionized shadowed region.

### 7.5.2. Neutral high density clumps

In what follows we will propose the presence of high density clumps inside the ionized layer left behind by the advancing ionization front. In the model we propose (illustrated in cartoon form in Figure 14) the clumps would not be permanent, rather, they would exist in the ionized layer only until they are destroyed by photoevaporation. The cool columns of gas behind them would then come to the higher equilibrium  $T_e$  appropriate for illumination by  $\theta^1$  Ori C rather than diffuse LyC.

One can approximate the results of an ionization front advancing into a clumpy PDR, as described in § 7.4. We don’t know the velocity of this advance. It must be small, because the tracers of the ionization front ([O II] and [S II]) are blueshifted  $2.5 \text{ km s}^{-1}$  with respect to the

PDR tracers (CO, C II) (O’Dell 2001a). This blueshift is probably due to the hot gas tracers coming from a layer that has already been accelerated by the pressure gradient, rather than being the result of  $\theta^1$  Ori C moving away from the PDR. The radial velocity of  $\theta^1$  Ori C is highly uncertain because of variability probably arising in the extended atmosphere of the star. It is unlikely that this star is moving at a high velocity with respect to the other cluster stars and their velocity is the same as the PDR (O’Dell 2001a) within the uncertainty of 3 km s<sup>-1</sup>. In the discussion below we will assume that the ionization front is advancing into the PDR at a rate of 2 km s<sup>-1</sup>, but it should be recognized that this could be off by a factor of two. In § 7.5 we showed that the fluctuations in the surface brightness of the nebula indicate structure with a height of about 0.025 pc. This would mean that the characteristic clump will have been illuminated by LyC radiation for about 1.3x10<sup>4</sup> years, which we will call the kinematic age.

If we can determine the column density and rate of loss of atoms per unit time and area, we can calculate the time that the clumps can survive photoevaporation and have a check on our basic model. If the clump diameters are about 0.0044 pc (corresponding to 2'') and the densities are 3x10<sup>6</sup> cm<sup>-3</sup> (Young Owl et al. 2000) the average column density of a clump would be 2.8x10<sup>22</sup> atoms cm<sup>-2</sup>. The corresponding mass would then be about 7x10<sup>30</sup> g).

The photoevaporation rate for these clumps will be very similar to those of the proplyds, which Henney et al. (2002) have shown to be 8x10<sup>-7</sup> M<sub>⊙</sub> yr<sup>-1</sup>. Since these objects are comparable in size to the clumps at the ionization front, their average rate of loss of atoms is relevant, this being 2x10<sup>11</sup> atoms cm<sup>-2</sup> s<sup>-1</sup>. In this case, the lifetime of the clumps would be about 5,000 yrs. However, the proplyd measured by Henney et al. (2002) must be much closer to  $\theta^1$  Ori C than the ionization front, so that the rate of loss has been overestimated and the survival age of the clumps underestimated. This means that the survival age of the clumps and their kinematic ages are compatible. They are, however, close enough that the process involved must be a dynamic one, with any one clump surviving for only about 10<sup>4</sup> years, but the number of clumps present at any time would be about constant as new clumps are revealed by the advancing ionization front.

We can estimate the effect of these shadowed regions if we know their emissivities and volumes. If the shadowed regions exist long enough that dynamical equilibrium is established with their surroundings (C98), then their volume emissivity will be four times that of the ambient lower density and higher  $T_e$  gas. If pressure equilibrium is not established, then the emissivity increase will be about two times that of the ambient gas. If one interprets the non-JET fluctuations in the extinction corrected H $\alpha$  surface brightness (Figure 7) as being due to knots at various distances from  $\theta^1$  Ori C, then they lie in a range of about 0.025 pc or

11", which is comparable to the emissivity scale-height of 15" derived in § 7.2. This means that the shadowed regions occur within the zone where most of the emission occurs.

To calculate the contribution to  $t^2(\text{O}^+)$  and  $t^2$  due to the shadows behind these clumps we need an estimate of the fraction of the emission produced in the shadowed regions. Assuming: a) the typical clump density to be  $N_e = 3 \times 10^6 \text{ cm}^{-3}$ , b) the average density of the ionized media to be  $N_e = 5 \times 10^3 \text{ cm}^{-3}$ , and c) that half of the ionized matter originated from the photoevaporation of these clumps, it follows that the volume originally occupied by the clumps must be about 1/1200 of the total volume. However, the shadowed volume is larger than the volume occupied by the clumps; we know that the shadows are approximately 0.025 pc long, while each clump is approximately 0.0044 pc across, so the shadowed volume can amount to approximately 1/200 of the volume of the region closest to the main ionization front, before these clumps are photoevaporated. Since these clumps survive long enough to cast 0.025 pc shadows, and the emissivity scale-height of the Orion Nebula is of 0.034 pc the total volume of the shadowed regions is about 1/250 of the effective emitting volume.

There are three possible physical conditions in the shadowed regions: a) that they are completely neutral, in this case they will not contribute to  $t^2(\text{O}^+)$  nor to  $t^2$ ; b) that they are completely ionized, but not in pressure equilibrium with their surroundings, then their contribution to  $t^2(\text{O}^+)$  would be about 0.0038 and to  $t^2$  of about 0.0016; and c) that they are completely ionized and in pressure equilibrium with their surroundings, then their contribution to  $t^2(\text{O}^+)$  would be about 0.0075 and to  $t^2$  of about 0.0032. The contribution of the shadows, including the shadows of the clumps and of the proplyds, amounts to  $0.009 \lesssim t^2(\text{O}^+) \lesssim 0.017$ , that corresponds to  $0.0043 \lesssim t^2 \lesssim 0.0075$ . Note that in the shadowed regions oxygen is either neutral or once ionized, and that therefore the shadowed regions do not contribute to the  $t^2(\text{O}^{++})$  value.

It can be shown that the ionized part of the proposed clumps has a very small effect on  $t^2$ . The clumps are expected to be close to the PDR, and their ionized part will have a larger density than the interclump medium, so we expect the oxygen in the ionized fraction of the clumps to be singly ionized. Additionally the clumps cover a total solid angle of about 0.03 steradians, and therefore absorb less than 1/400 of the ionizing photons, about 1/800. This implies that their emissivity amounts to about 1/800 of the total emissivity of the nebula and that the physical conditions in the high density photoevaporated region will produce a negligible effect in the increase of  $t^2(\text{O}^+)$  or  $t^2$ .

## 7.6. Can the clumpy model for the Ionized Layer explain the Anomalous Line Broadening in Orion?

There is an unexplained component of line broadening in the Orion Nebula that may be explained by the clumpy model for the ionized layer that we propose. This anomaly first surfaced with Castañeda’s (1988) study of [O III], and remained with the inclusion of other massive ions ([O II], Jones 1992; [O I], O’Dell & Wen 1992; [S III], Wen & O’Dell 1993). After quadratic subtraction of the instrumental, thermal, and turbulent components of broadening, there remains a large and unexplained line width having  $\text{FWHM} \simeq 10 \text{ km s}^{-1}$ . The large thermal width of the H I lines makes it difficult to accurately determine the extra width there, however, Wilson, et al.’s (1997) study of the H64 $\alpha$  line indicates an unexplained broadening component (called the turbulent velocity in their paper) of  $19.6 \pm 0.9 \text{ km s}^{-1}$ .

This extra broadening component has been re-addressed using spectra made with the Keck telescope for the study of proplyds and their jets (Henney & O’Dell 1999, Bally, O’Dell, & McCaughrean 2000. The Keck data were very useful as they have the highest velocity resolution ( $6 \text{ km s}^{-1}$ ) of any of the optical wavelength studies and allow examination of all of the primary lines of [O I], [O III], [S II], [N II], He I, H $\alpha$ , and H $\beta$  at exactly the same positions. Samples were taken from 14'' long spectra centered on 137-349, 150-353, 163-357, 170-337, 177-341, 182-413, and 244-440 (the designation system is described in O’Dell & Wen 1994) and 28'' long spectra taken at the positions 137-349, 150-353, and 163-357. After correction for instrumental, thermal, and turbulent (assumed to be  $1 \text{ km s}^{-1}$ ) broadening, the remaining line widths (FWHM in  $\text{km s}^{-1}$ ) were H $\alpha$   $20.9 \pm 1.3$ , H $\beta$   $18.8 \pm 2.2$ , He I 5876 Å  $18.4 \pm 2.9$ , [N II] 6583 Å  $10.6 \pm 1.4$ , [O I] 6300 Å  $9.0 \pm 2.1$ , [O III] 5007 Å  $13.0 \pm 3.7$ , [O III] 4959 Å  $11.3 \pm 2.1$ , [S II] 6731 Å  $11.3 \pm 2.4$ , and [S III] 6312 Å  $11.8 \pm 1.9$ . The only source of [O II] data are those found in the thesis of Michael Jones (1992) who found for  $10.5 \pm 2.5$  for the central 80''x 80''. The longer Keck slit spectra were subjected to a separate analysis using various fractions of the total slit length and no variation of the results were seen, i.e. there was not a relation between sample size and the residual line width. The radio (H64 $\alpha$ ,  $19.6 \pm 0.9$ ) and optical (H $\alpha$ ,  $20.9 \pm 1.3$  and H $\beta$ ,  $18.8 \pm 2.2$ ) are in agreement within their individual uncertainties.

The unexplained broadening in the emission lines that arise from the lower temperature component of the nebula is twice that of lines arising from the higher temperature component. We see that the recombination lines of H I and He I that preferentially come from cool regions have a clearly larger unexplained width (average  $19.4 \text{ km s}^{-1}$ ) than the collisionally excited forbidden lines that preferentially come from hot regions (average  $10.9 \text{ km s}^{-1}$ ). This strongly argues against the broadening arising from Alfvén waves (OD2001) since they would have little dependence upon  $T_e$ . The explanation certainly does not lie with there being a

systematic difference in  $T_e$ , because the sense of the correlation is opposite to that expected.

The clearcut differences in the extra broadening in collisional and recombination lines is probably related to the the mechanism giving rise to the temperature inhomogeneities. Can the broadening be due to the clumpy structure that we argue can explain the temperature inhomogeneities? O'Dell & Wen (1992) argue that clumps having sizes of less than  $2.3''$  could produce the extra broadening, but this argument was made before knowledge of the larger broadening of the hydrogen lines. The steady process of destruction of the clumps by photoevaporation would certainly give rise to flows away from the clumps. However, the line broadening due to this should selectively be a blueward distortion of the integrated line-of-sight line profile, except for the final stage of destruction, when material would be flowing in all directions. However, the initial phase of a shadowed region would be accompanied by material flowing inward towards the low pressure zone that would exist when the shadowed  $T_e$  drops and the shadowed region is moving towards a state of hydrostatic equilibrium. It is obvious that these situations need to be theoretically modeled. Although it is not now possible to quantitatively link them, it is likely that the explanation of the electron temperature fluctuations and the line widths are related.

## 8. Conclusions

From our  $T_e(\text{O}^{++})$  map of the Orion Nebula, that includes  $1.5 \times 10^6$  independent temperature determinations, we have found that  $t_A^2(\text{O}^{++}) = 0.008$ .

From our  $t_A^2(\text{O}^{++})$  value, together with geometrical considerations and other observations in the literature, we estimate that  $t^2(\text{O}^{++}) = 0.021$ . Note that the total  $t^2(\text{O}^{++})$  is larger than  $t_A^2(\text{O}^{++})$  because in addition to the variations across the plane of the sky it includes the temperature variations along the line of sight.

From our  $t^2(\text{O}^{++})$  value and comparisons between the temperatures in the low- and high-ionization zones, the  $\text{O}^+$  and  $\text{O}^{++}$  zones, we find that  $t^2(\text{H II}) = 0.028 \pm 0.006$ .  $t^2(\text{H II})$  is different to  $t^2(\text{O}^{++})$  because in addition to the variations in the  $\text{O}^{++}$  zone includes the variations in the  $\text{O}^+$  zone and the difference in the average temperature between both zones. Our derived  $t^2(\text{H II})$  value is 7 times higher than those obtained from homogeneous one-dimensional photoionization models of the Orion Nebula.

A combination of sources needs to be found to explain the large  $t^2$  values observed in the Orion Nebula. Many possible causes of temperature variations have been discussed in the literature like: density variations, deposition of mechanical energy, deposition of magnetic energy, presence of shadowed regions, chemical inhomogeneities, dust heating, and transient

effects due to changes in the ionizing flux.

From observations of variations in surface brightness, columnar electron temperature, radial velocity, and ionization, we have established the presence of significant small scale structure at the 1-5 arc sec level. The small scale velocity and ionization structures are probably strongly linked with the temperature structure.

The presence of this small scale structure is compatible with a new model for the structure of the nebula near the ionization front. We posit that this front is advancing into the highly clumpy photodissociation region revealed by radio and infrared observations. These clumps possess ionized shadows that are of low  $T_e$ . A quasi-static equilibrium exists in which any one clump survives the process of photoevaporation only for a short time. The process may be common to most H II regions which have a portion that is ionization bounded. There is an unexplained component of line broadening in the Orion Nebula that may be explained by the clumpy model for the ionized layer that we propose.

We have discussed the presence of shadowed regions due to proplyds and to high density clumps near the PDR. We estimate that the shadowed regions can contribute  $0.0043 \lesssim t^2 \lesssim 0.0075$  to the total  $t^2$  value, which together with the homogeneous one dimensional ionization structure provide only from about one third to about half of the observed  $t^2$  value. Additional sources of temperature variations are needed to explain the total  $t^2$  observed value. Moreover, since in the shadowed regions O is only once ionized, these regions could be responsible for temperature variations in the  $O^+$  zone, but not in the  $O^{++}$  zone, and since the  $t^2(O^{++})$  value is very large we need one or several additional sources of temperature variations to explain it.

There is an anomalous broadening mechanism operating in the Orion Nebula which is unexplained. It broadens H and He recombination line emission by about  $19 \text{ km s}^{-1}$  and the forbidden line emission from heavy ions by about  $11 \text{ km s}^{-1}$ . Since these two types of lines selectively rise from the low and high temperature components along a line of sight, it appears likely that this process is related to the  $t^2$  problem.

Michael Richer and Will Henney provided valuable support in obtaining the high velocity resolution spectra at the Mexican National Observatory at San Pedro Martir. Will Henney also provided several useful comments on an earlier version of this paper. Takao Doi kindly shared before publication the results of his Orion Nebula radial velocity program, which allowed us to generate Figure 8 and Figure 9. Henney also provided observations on the expected rate of motion of the ionization front in the Orion Nebula. Gary J. Ferland provided estimates for the heating rates. Christopher A. Coco measured the Keck spectra line widths as part of his senior thesis at Rice University. The authors are grateful to Patrick Hartigan



of Rice University and Robert Rubin of the Ames Research Center for discussions on some aspects of this work. CRO's work was supported in part by grant GO-9141 from the STScI to Vanderbilt University. MP's work was supported in part by grant IN 114601 from DGAPA UNAM.

## REFERENCES

- Baldwin, J. A., Ferland, G. J., Martin, P. G., Corbin, M. R., Cota, S. A., Peterson, B. M., & Slettebak, A. 1991, *ApJ*, 374, 580 (B91)
- Bally, J., O'Dell, C. R., & McCaughrean, M. J. 2000, *AJ*, 119, 2919
- Brand, P. W. J. L. 1981, *MNRAS*, 197, 217
- Buisson, H., Fabry, C., & Bourget, H. 1914, *ApJ*, 40, 241
- Cantó, J., Goudis, C., Johnson, P. G., & Meaburn, J. 1980, *A&A*, 85, 128
- Cantó, J., Raga, A., Steffen, W., & Shapiro, P. R. 1998, *ApJ*, 502, 695 (C98)
- Capriotti, E. R. 1973, *ApJ*, 179, 495
- Castañeda, H. O. 1988, *ApJS*, 67, 93
- Esteban, C. 2002, *Rev. Mexicana Astron. Astrofis. Ser. Conf.*, 12, 56
- Esteban, C., Peimbert, M., Torres-Peimbert, S., & Escalante, V. 1998, *MNRAS*, 295, 401 (EPTE98)
- Ferland, G. J. 2001, *PASP*, 113, 41
- García-Segura, G., & Franco, J. 1996, *ApJ*, 469, 171
- Garnett, D.R. 1992, *AJ*, 103, 1330.
- Gruenwald, R., & Viegas, S.M. 1992, *ApJS*, 78, 153
- Hartigan, P. 1999, *ApJ*, 526, 274
- Henney, W. J. 1998, *ApJ*, 503, 760
- Henney, W. J., & O'Dell, C. R. 1999, *AJ*, 118, 2350
- Henney, W. J., O'Dell, C. R., Meaburn, J., Garrington, S. T., & López, J. A. 2002, *ApJ*, 566, 315
- Hogerheijde, M. R., Jansen, D. J., & van Dishoeck, E. F. 1995, *A&A*, 294, 792
- Holtzman, J. A., Burrows, C. J., Castertano, S., Hester, J. J., Trauger, J. T., Watson, A. M., & Worthey, G. 1995, *PASP*, 107, 1065

- Jones, M. R. 1992, PhD thesis, Rice Univ., Houston, TX
- Kirkpatrick, R. C. 1972, *ApJ*, 176, 381
- Liu, X.-W. 2002a, *Rev. Mexicana Astron. Astrofis. Ser. Conf.*, 12, 70
- Meaburn, J., Blundell, B., Carling, R., Gregory, D. F., Keir, D., & Wynne, C. G. 1984, *MNRAS*, 210, 463
- O'Dell, C. R. 1998a, *AJ*, 115, 263
- O'Dell, C. R. 1998b, *AJ*, 116, 1346
- O'Dell, C. R. 2000, *AJ*, 119, 2311
- O'Dell, C. R. 2001a, *PASP*, 113, 29
- O'Dell, C. R. 2001b, *ARAA*, 39, 99 (OD2001)
- O'Dell, C. R. 2002, *Rev. Mexicana Astron. Astrofis. Ser. Conf.*, 12, 12
- O'Dell, C. R., & Doi, T. 1999, *PASP*, 111, 1316 (OD99)
- O'Dell, C. R., & Doi, T. 2003, *AJ*, 125, 277
- O'Dell, C. R., Hartigan, P., Lane, W. M., Wong, S. K., Burton, M. G., Raymond, J., & Axon, D. J. 1997, *AJ*, 114, 730 (O97)
- O'Dell, C. R., Hartigan, P., Bally, J., & Morse, J. A. 1997, *AJ*, 114, 2016
- O'Dell, C. R., & Hubbard, W. B. 1965 *ApJ*, 142, 591
- O'Dell, C. R., Walter, D. K., & Dufour, R. J. 1992, *ApJ*, 399, L67
- O'Dell, C. R., & Wen, Z. 1992, *ApJ*, 387, 229
- O'Dell, C. R., & Wen, Z. 1994, *ApJ*, 436, 194
- O'Dell, C. R., & Yusef-Zadeh, F. 2000, *AJ*, 120, 382
- Osterbrock, D. E., Tran, H. D., Veilleux, S. 1992, *ApJ*, 389, 305
- Peimbert, A. 2003, *ApJ*, 584, 735
- Peimbert, A., Peimbert, M., & Luridiana, V. 2002, *ApJ*, 565, 668
- Peimbert, M. 1967, *ApJ*, 150, 825
- Peimbert, M. 1995, in *The Analysis of Emission Lines*, eds. R. E. Williams, & M. Livio (Cambridge), 165
- Peimbert, M. 2002, *Rev. Mexicana Astron. Astrofis. Ser. Conf.*, 12, 275
- Peimbert, M., Peimbert, A., & Ruiz, M. T. 2000, *ApJ*, 541, 688
- Peimbert, M., Storey, P. J., & Torres-Peimbert, S. 1993, *ApJ*, 414, 626.

- Peimbert, M., & Torres-Peimbert, S. 1977, MNRAS, 179, 217
- Rubin, R. H., Bhatt, N. J., Dufour, R. J., Buckalew, B. A., Barlow, M. J., Liu, X.-W., Storey, P. J., Balick, B., Ferland, G. J., Harrington, J. P., & Martin, P. G. 2002, MNRAS, 334, 777 (R2002)
- Rubin, R. H., Martin, P. G., Dufour, R. J., Ferland, G. J., Blagrove, K. P. M., Liu, X.-W., Nguyen, J. F., & Baldwin, J. A. 2003, MNRAS, in press, (astro-ph/0212244), (R2003)
- Stasińska, G. 2002, Rev. Mexicana Astron. Astrofis. Ser. Conf., 12, 62
- Tauber, J. A., Goldsmith, P. F., & Dickman, R. L. 1991, ApJ, 375, 635
- Torres-Peimbert, S., & Peimbert, M. 2003, in Planetary Nebulae and Their Role in the Universe, IAU Symposium 209, in press, (astro-ph/0204087)
- Van Blerkom, D., & Army, T. T. 1972, MNRAS, 156, 91
- van der Werf, P. P., Stutzki, J., Sternberg, A., & Krabbe, A. 1996, A&A, 313, 633
- Vannier, L., Lemaire, J. L., Field, D., Pineau des Forêts, G. Pijpers, F. P., & Rouan, D. 2001, A&A, 366, 651
- Vishniac, E. T. 1994, ApJ, 428, 186
- von Hörner, S. 1951, ZAp, 30, 17
- Walter, D. K., O'Dell, C. R., Hu, X., & Dufour, R. J. 1995, PASP, 107, 686
- Wen, Z., & O'Dell, C. R. 1993, ApJ, 409, 262
- Wen, Z., & O'Dell, C. R. 1995, ApJ, 438, 784 (WO95)
- Williams, R. J. R. 1999, MNRAS, 310, 789
- Wilson, O. C., Münch, G., Flather, E. M., & Coffeen, M. F. 1959, ApJS, 4, 199
- Wilson, T. L., Filges, L, Codella, C., Reich, W., & Reich, P. 1997, A&A, 327, 1177
- Young Owl, R. C., Meixner, M. M., Wolfire, M., Tielens, A. G. G. M., & Tauber, J. 2000, 540, 886

Table 1. Filter and WFPC2 Characteristics

Filter	F437N	F469N	F487N	F502N	F547M	F656N	F658N
$E_{\text{filter}}^{\text{a}}$	16.56	17.40	19.87	22.79	601.9	22.0 4	31.19
$T_{\text{ll}}^{\text{filter b}}$	0.50	0.52	0.59	0.64	—	0.78	0.79
$T_{\text{sec}}^{\text{filter c}}$	0.005	—	—	—	—	0.24 <sup>d</sup>	0.045
$s^{\text{e}}$	0.061	0.074	0.084	0.091	0.125	0.145	0.145

<sup>a</sup>  $E_{\text{filter}} = \int_0^\infty T_\infty d\lambda$ =effective width of the filter in Å.

<sup>b</sup>  $T_{\text{ll}}^{\text{filter}}$ =transmission at primary line for the filter.

<sup>c</sup>  $T_{\text{sec}}^{\text{filter}}$ =transmission at the secondary line for the filter.

<sup>d</sup> This value is for the [N II] 6548 Å line, it is 0.055 at the three times stro nger [N II] 6583 Å line.

<sup>e</sup> The WFPC2+HST system throughput determined in 2001 June from Table 2.4 of the WF PC2 Instrument Handbook.

Table 1.  $t_A^2(\text{O}^{++})$ .

Region	Number of pixels ( $10^6$ )	$\langle T_c \rangle$	$t_A^2(\text{O}^{++})$
Region 1	0.51	9190	0.0117
Region 2	0.43	9390	0.0156
Region 3	0.34	9240	0.0050
Region 4	1.50	9250	0.0096
Region 5	1.09	9220	0.0084

Fig. 1.— This [O III] 5007 Å image from the data set illustrates the location of the WFPC2 field of view. The horizontal width of the image is 149" and the central intersection of the edges of the CCD detectors is at 5:35:14.2 -5:24:03 (2000). The vertical axis points north. The regions used for calibration and for comparison with spectroscopic and ionization changes are indicated.

Fig. 2.— This is the  $T_c$  image derived from the WFPC2 dataset for the field of view shown in Figure 1, at the same scale and orientation. Local values of  $T_c/10,000$  are shown as numbers like 0.93. The white open circles surround features that are “scars” caused by stars. Two proplyds that show high values of  $T_c$  are labeled (141-301, 182-413). Features associated with HH 202 and HH 269 are labeled and discussed in the text. The dark solid line lies over a diffraction spike caused by one of the vanes holding the secondary mirror of the HST. Features within CCD1 are suspect because of scattered light from  $\theta^1$  Ori C and other bright Trapezium stars. The black outlines depict the regions assessed for small scale changes in  $T_c$  as shown in Figure 3.

Fig. 3.— The regions outlined in Figure 2 are shown here in the same spatial orientation. A Poisson-noise-only image of 5.7 % noise is shown in the upper left. The display range has been adjusted to show the intermediate scale fluctuations in  $T_c$ . The pure noise field is 50"x 50". The northwest (NW) field is 37"x 40" and the southeast (SE) field is 76"x 76". The southwest (SW) field is 72"x 75" and its resolution is one half that of the other images, which are one pixel of 0.0996". Because the southeast region is about one fourth the surface brightness of the other fields, its data were averaged in bins of 2 x 2 pixels, thus making the expected noise comparable to that of the other images.

Fig. 4.— The results of a Fourier analysis of a section of the  $T_c$  image in CCD2 is shown as a power spectrum with noise subtracted in arbitrary units (ordinate) versus the size scale (L) in units of the coarser WFPC2 pixels of 0.0996". One sees the highest power in the smallest scales, although there is power even in the largest scale.

Fig. 5.— The same as Figure 4, except for a region selected from CCD4.

Fig. 6.— Histogram of the  $T_4(\text{O}^{++})$  columnar values from the pixels in region 5. Note that  $t_A^2(\text{O}^{++})$  cannot be obtained directly from this histogram as each pixel needs to be weighted by its emission measure, see text.

Fig. 7.— The surface brightness in the H $\alpha$  line, after correction for extinction by the radio-optical method of O'Dell & Yusef-Zadeh (2000), is shown as a function of distance (increasing numbers to the north) for the velocity sample region shown in Figure 1. The featured marked “JET” is the inner jet associated with HH 269 (O'Dell & Doi 2003).

Fig. 8.— The emission from four lines (from left,  $H\alpha$ ,  $[S\ II]$ ,  $[N\ II]$ ,  $[O\ III]$ ) are shown for the sample indicated in Figure 1, with north at the top. The additional thermal broadening of the  $H\alpha$  line causes its spectrum to be noticeably wider than the more massive ions. One sees a progression of fine scale motion as the volume of the emitting zone is decreased,  $H\alpha$ ,  $[O\ III]$ ,  $[N\ II]$ , and  $[S\ II]$ .

Fig. 9.— This linear, equal interval, contour plot shows the same spectral data as in Figure 8.

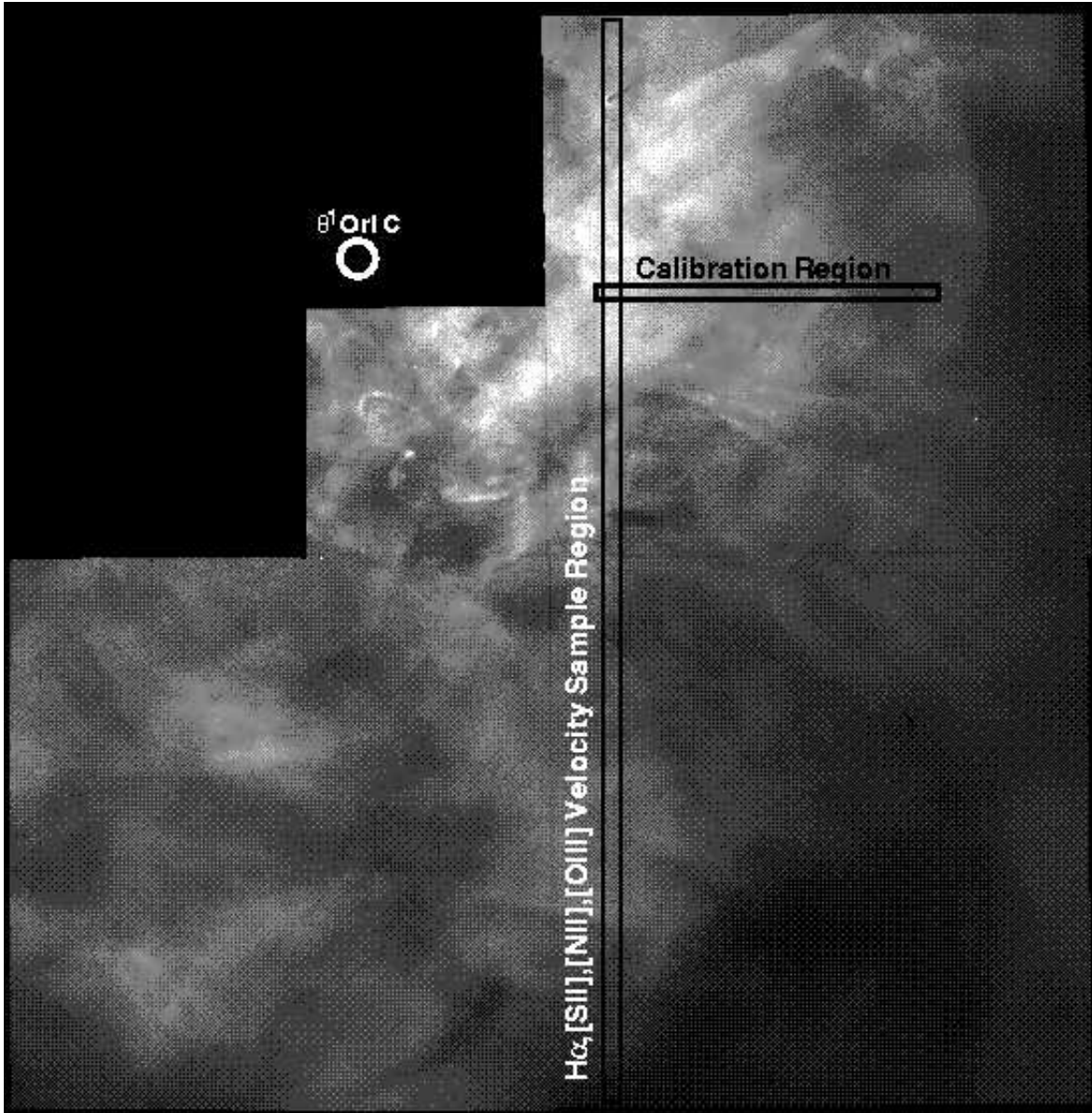
Fig. 10.— These figures show the same field of view as Figure 1. The left hand side shows the ratio of the signal in the F658N filter divided by the signal in the F656N filter. The right hand side shows the ratio of the signal in the F502N filter divided by the signal in the F587N filter. Both images are intended to show small scale ionization changes and to do this in a way insensitive to varying amounts of interstellar extinction.

Fig. 11.— This is a profile from the left hand portion of Figure 10 over the velocity sample section depicted in Figure 1. The location of the CCD seam between CCD3 and CCD4 is indicated, as is the location of the only star in the sample. Both of these features cause uncertainty in the line ratios and quantities derived from them.

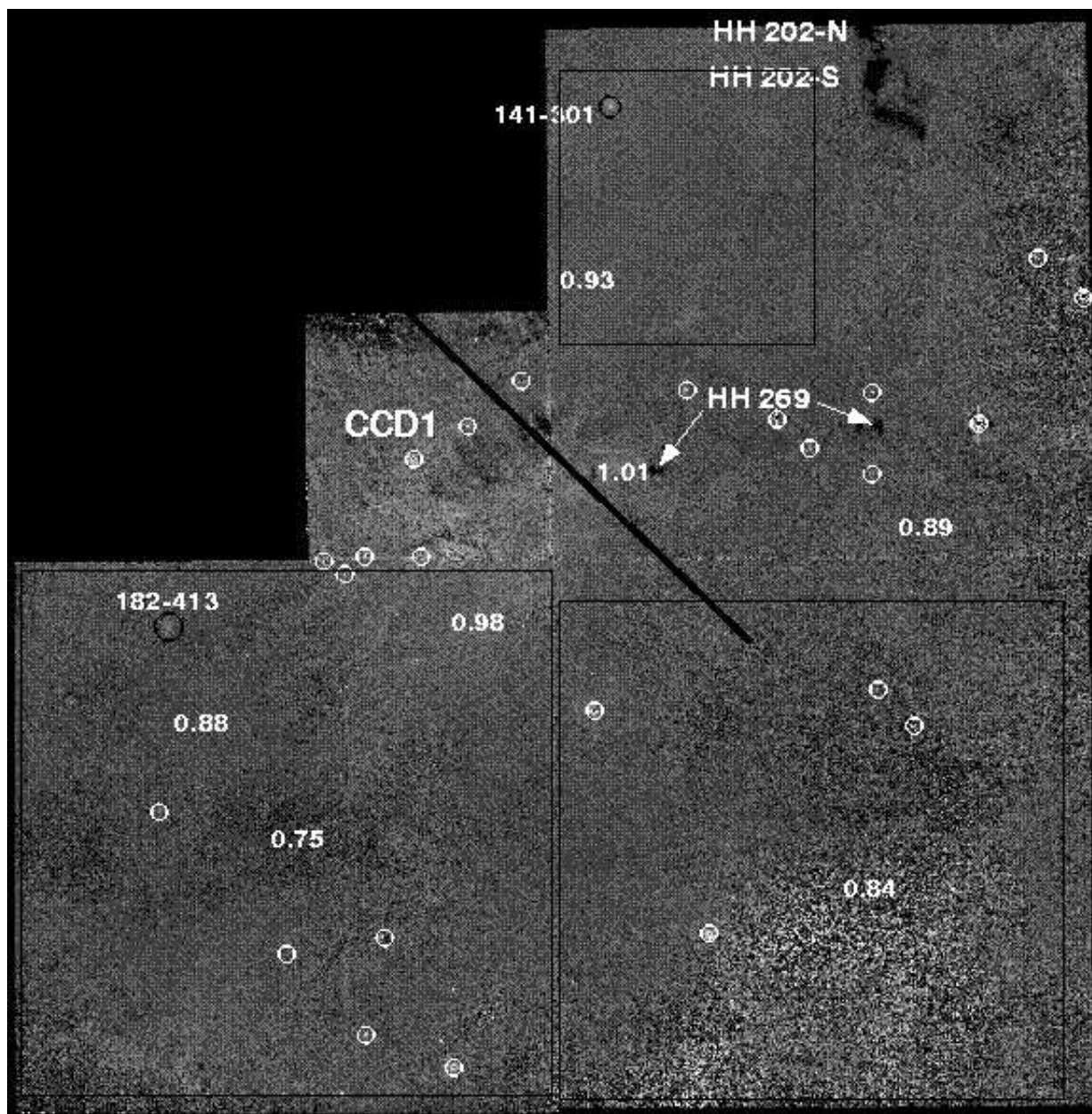
Fig. 12.— The same as Figure 11 except for the F658N/F656N ratio of signals.

Fig. 13.— The electron temperature in units of 10,000 K is shown in profile for the same section as the velocity samples in Figure 1.

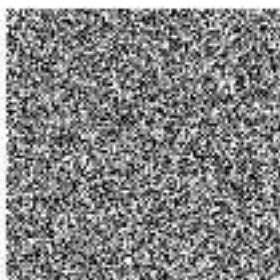
Fig. 14.— The proposed knotty model for the ionization front is presented here in cartoon form. Each knot would be subject to photoionization as soon as the average location of the ionization front has moved past it. Each knot would be brightest on the side facing  $\theta^1$  Ori C and would be destroyed by the process of photoevaporation. Prior to their destruction each would have produce a shadowed region photoionized only by diffuse LyC radiation and having an electron temperature about three-fifths that of the directly illuminated material.







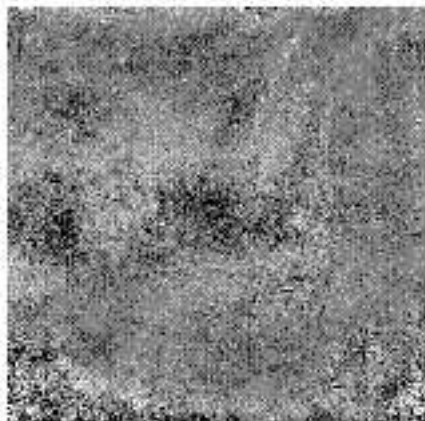
**5.7 % Noise +/- 1000 K**



**NW +/- 1000 K**

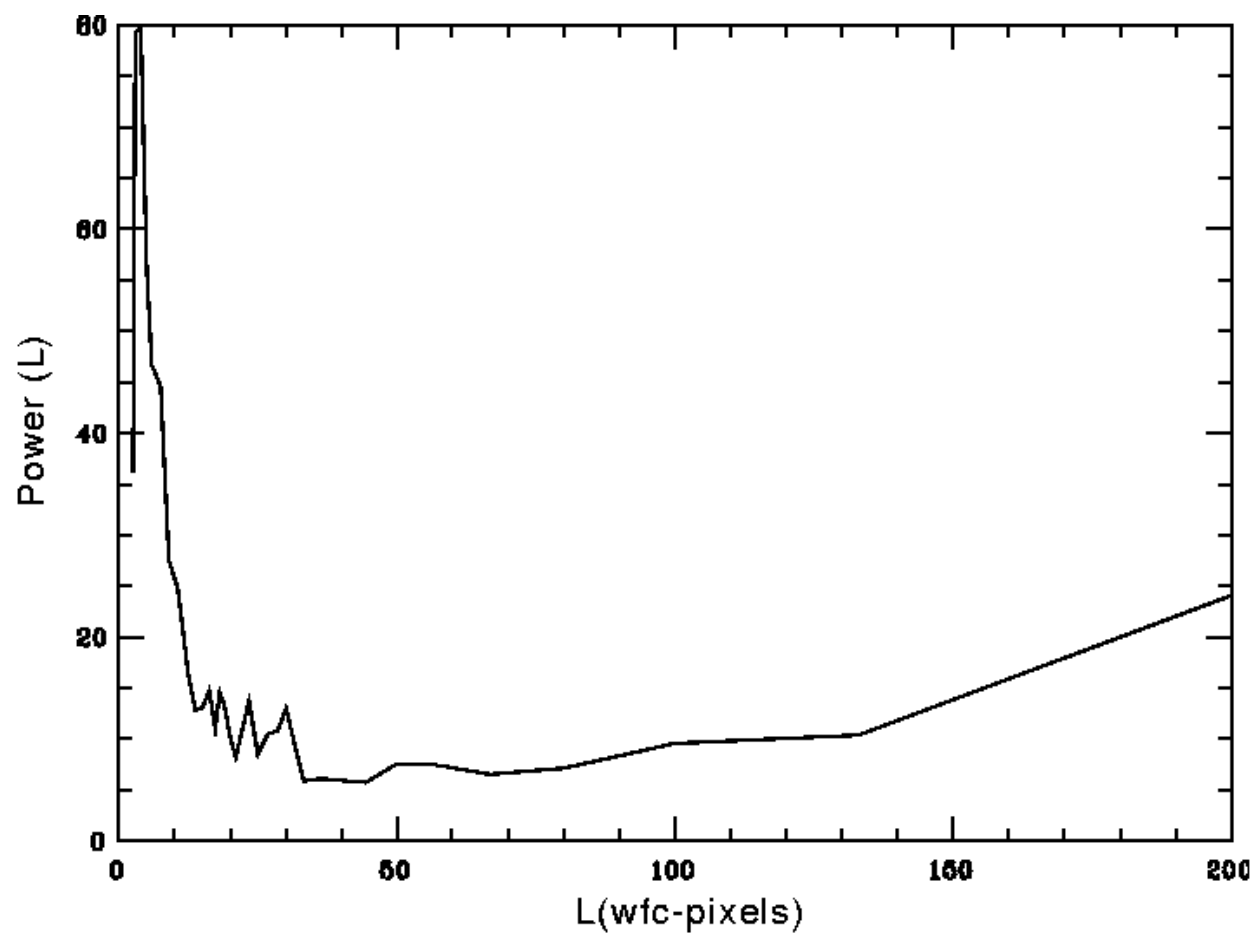


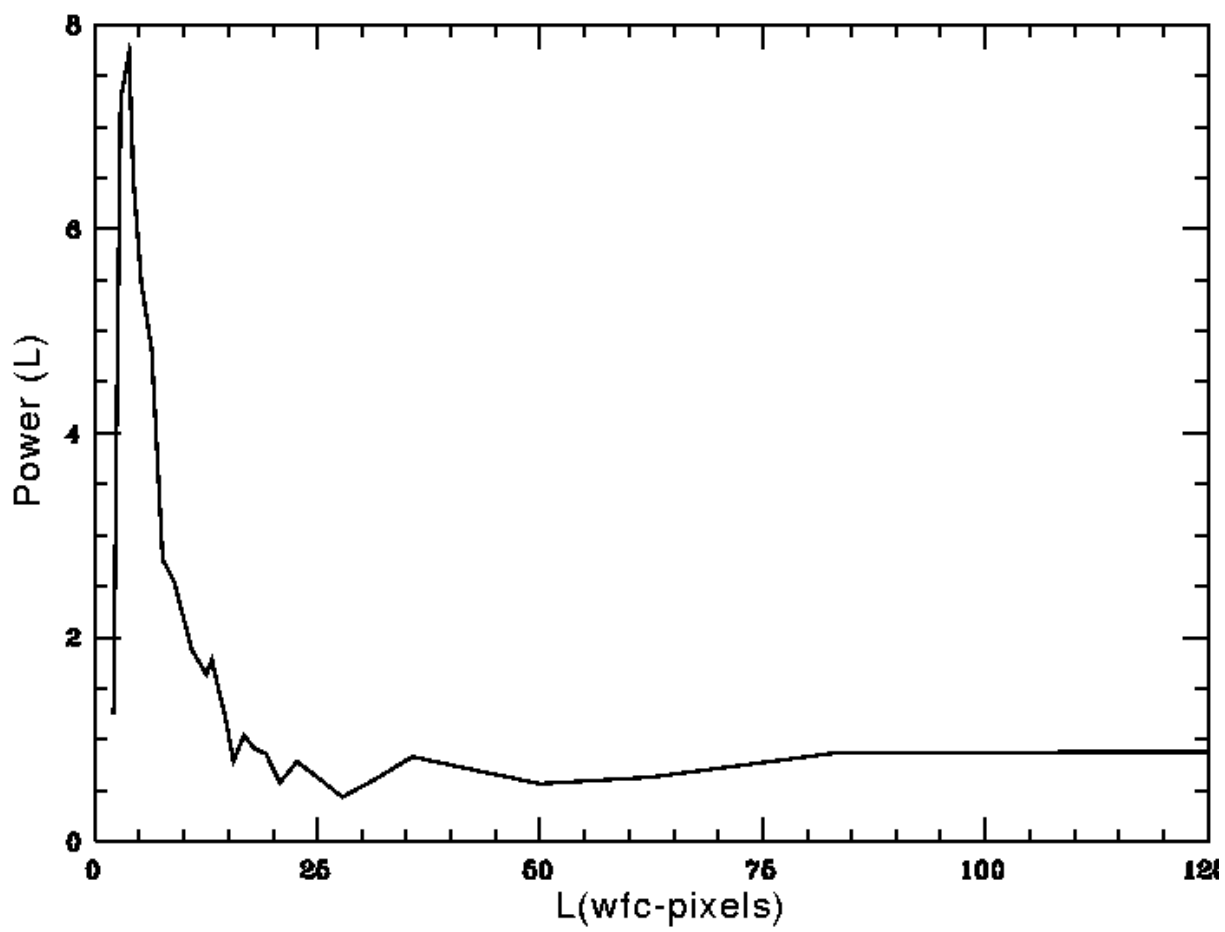
**SE +/- 1000 K**

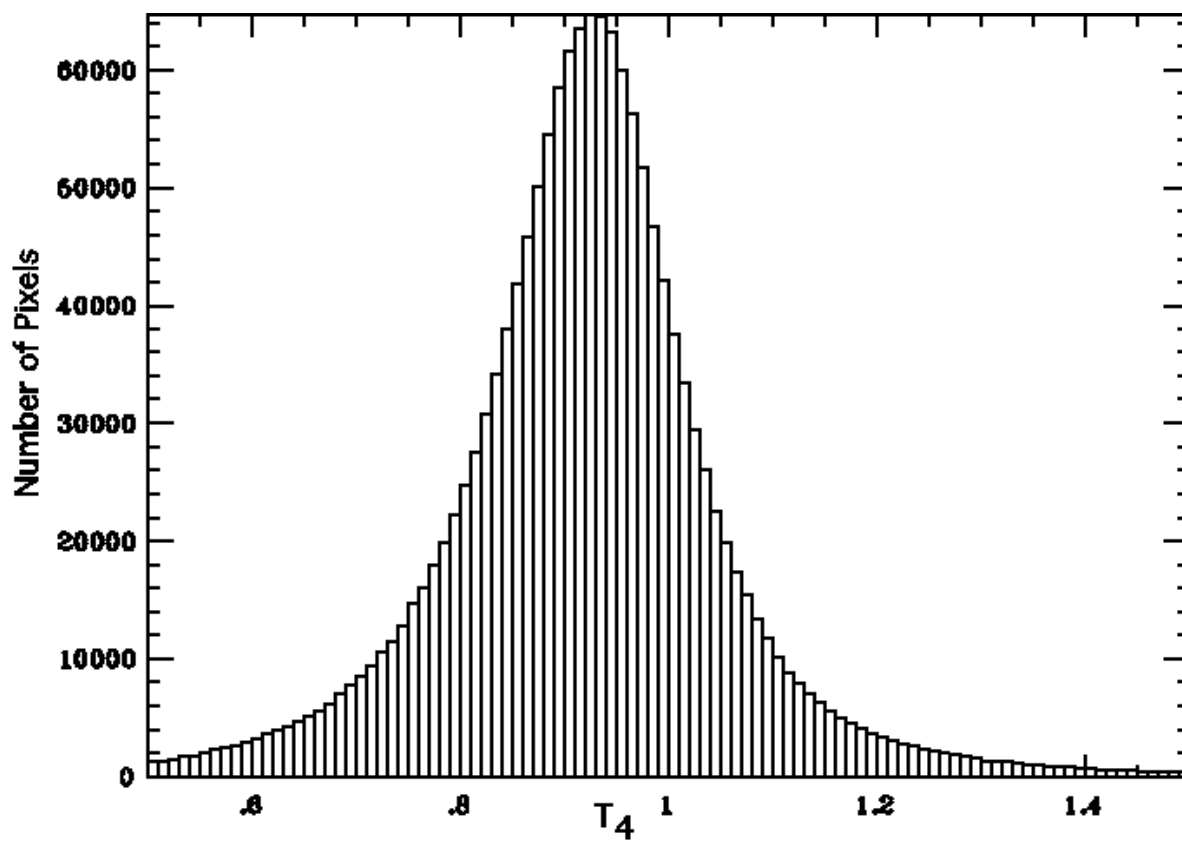


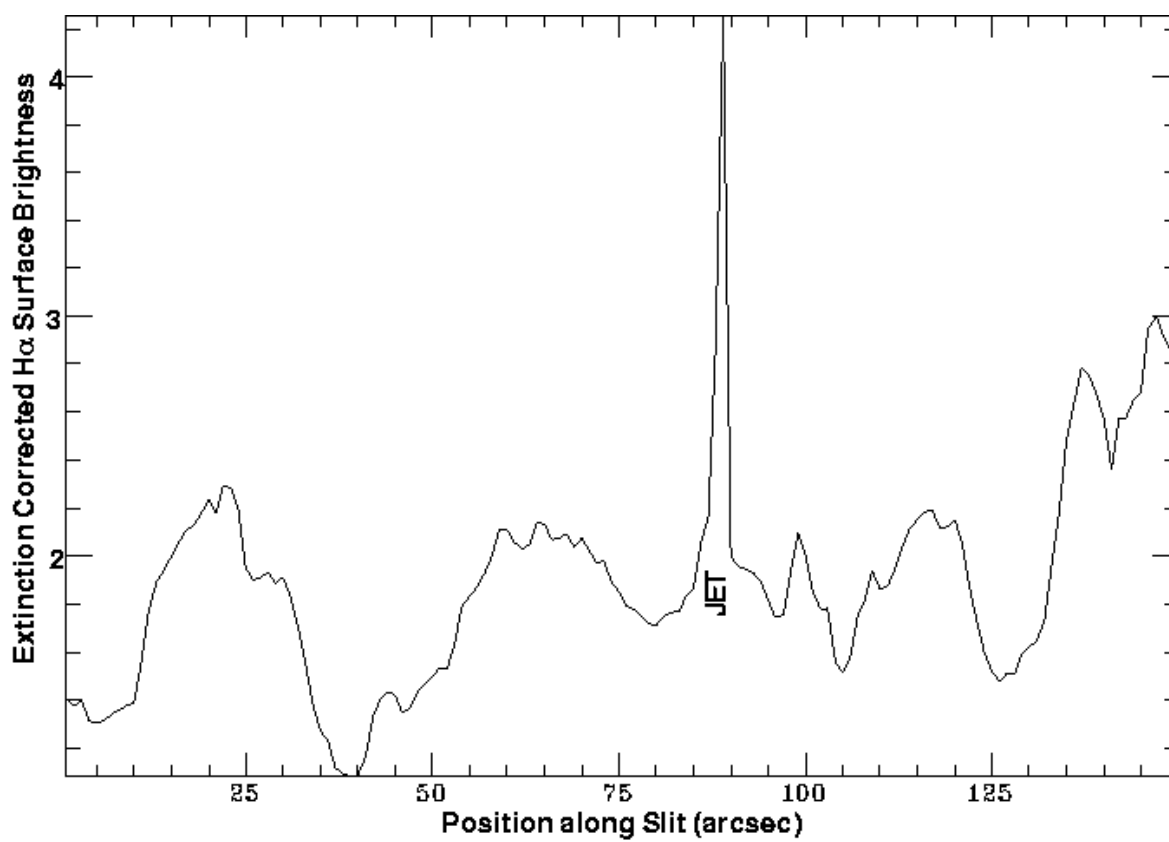
**SW +/- 1000 K**

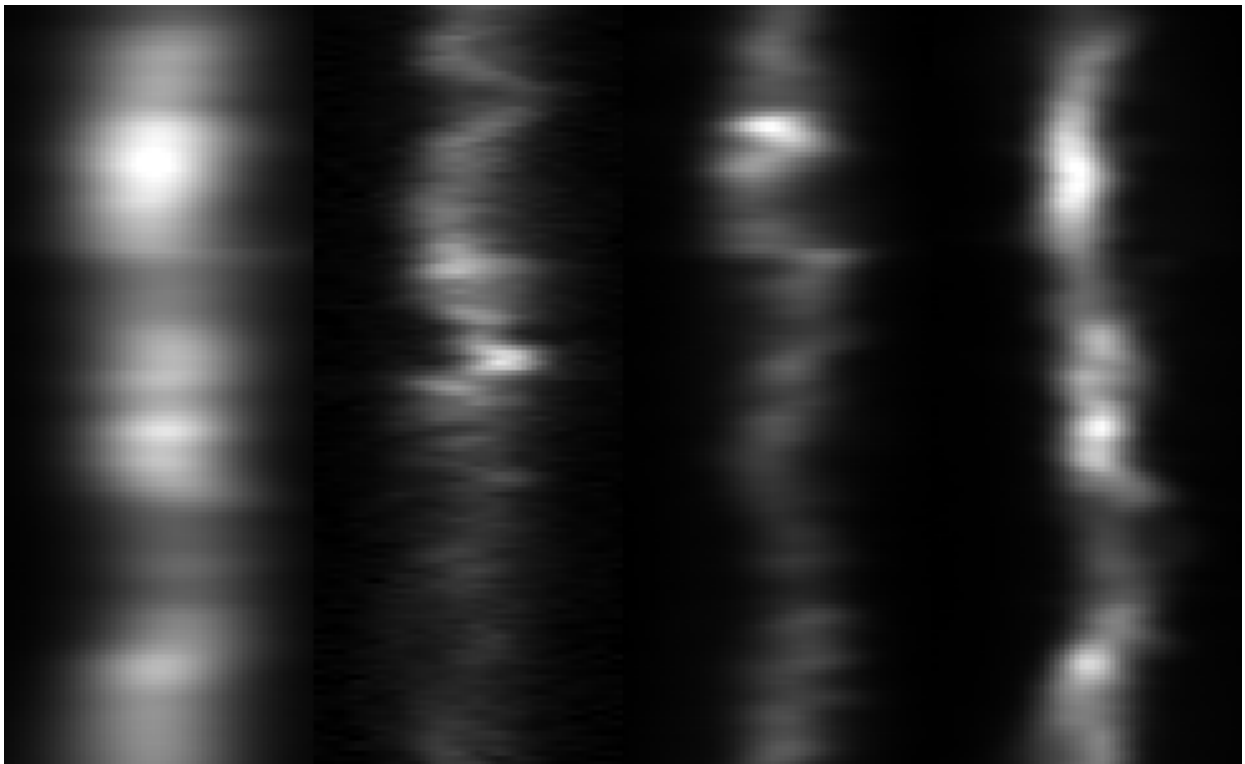


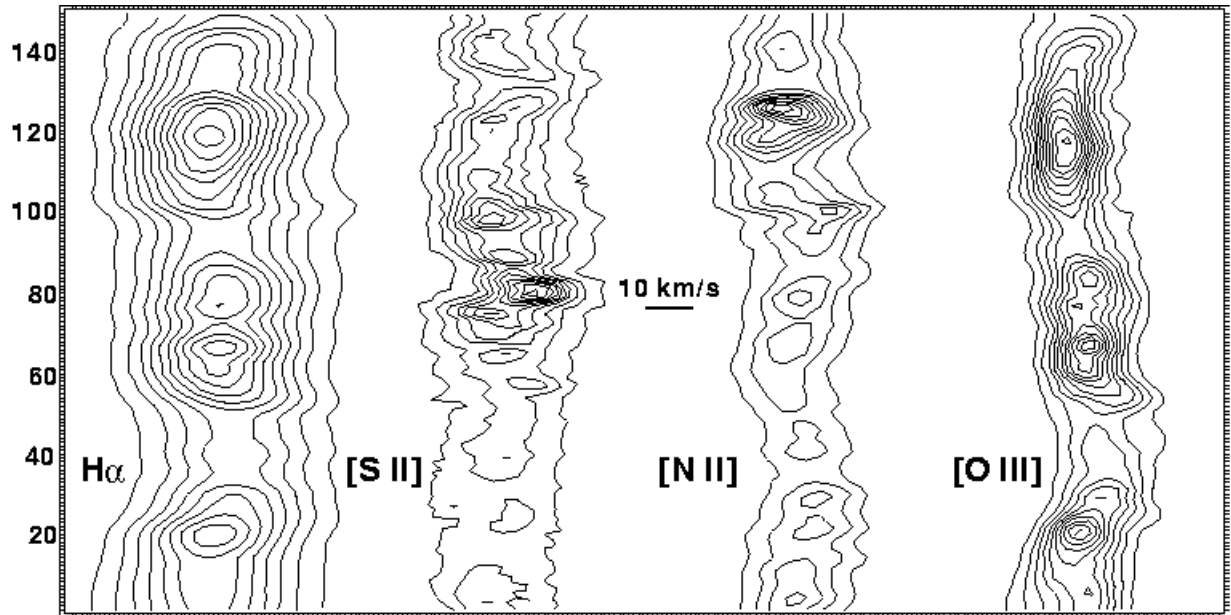




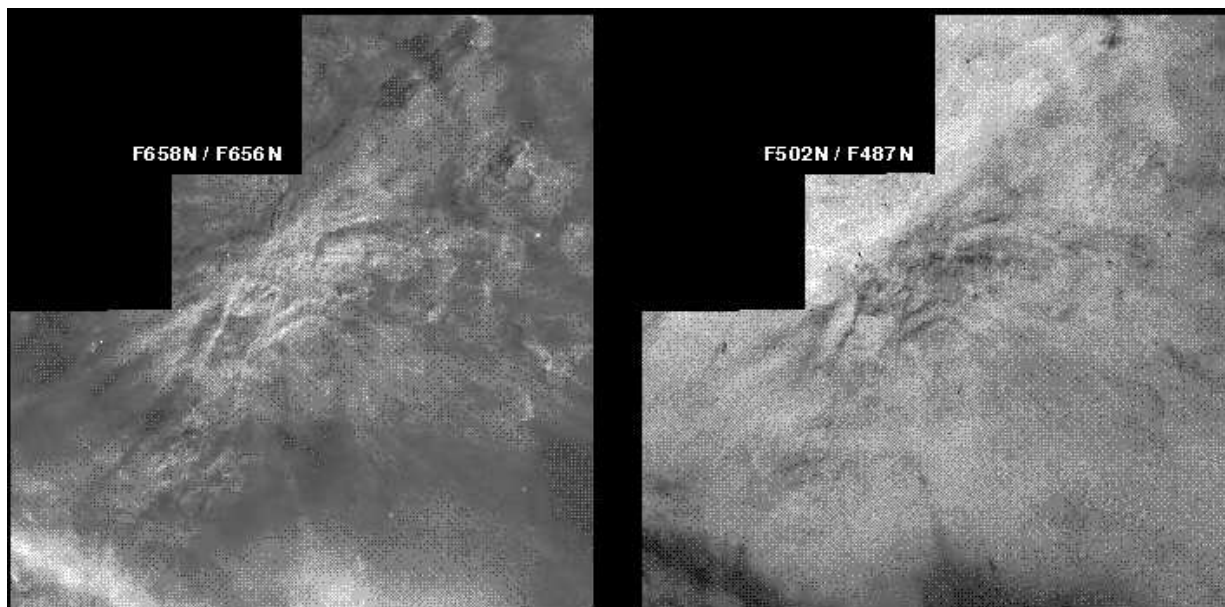


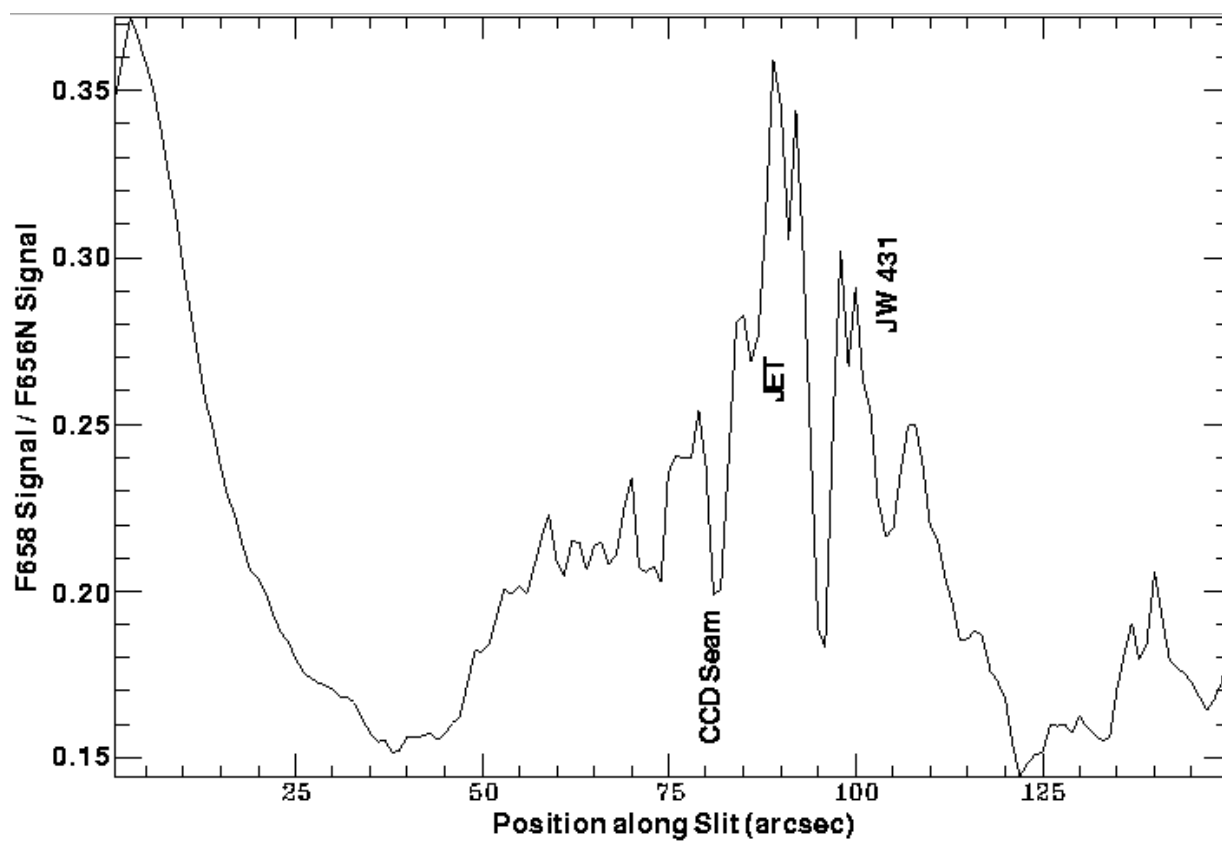


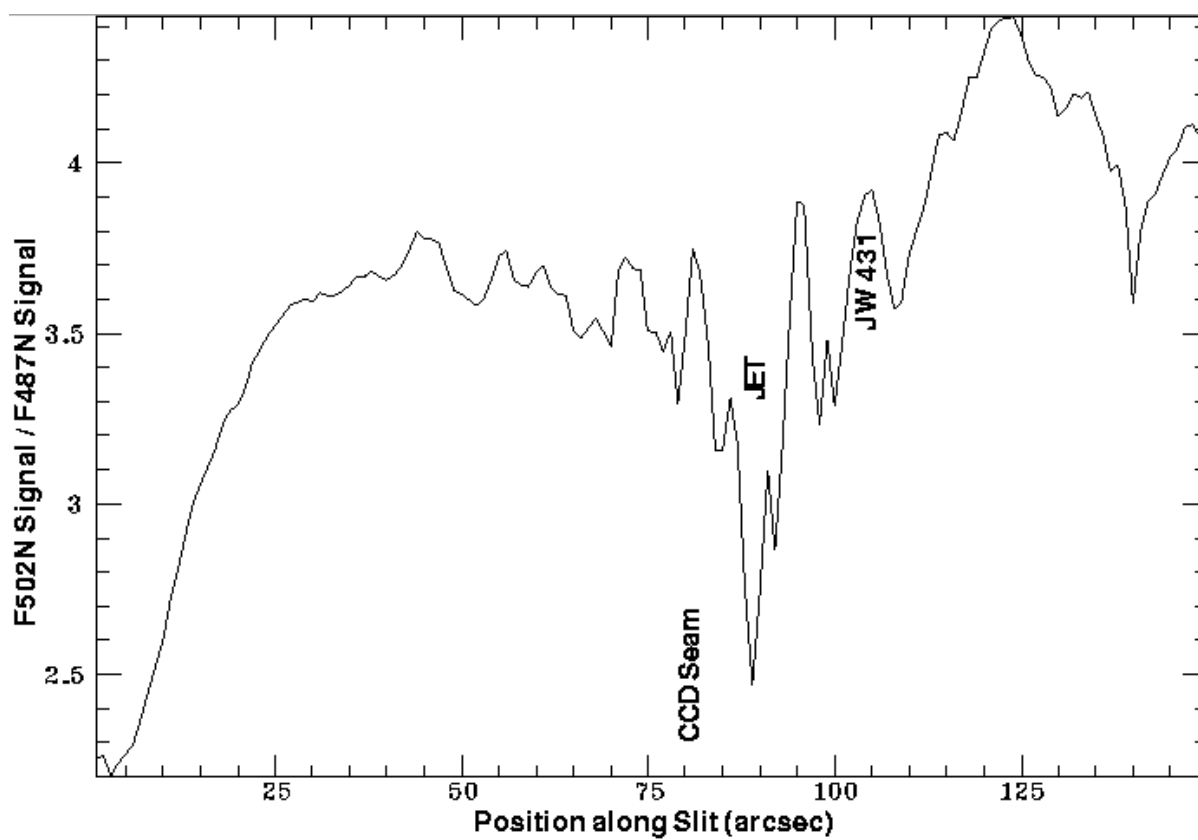


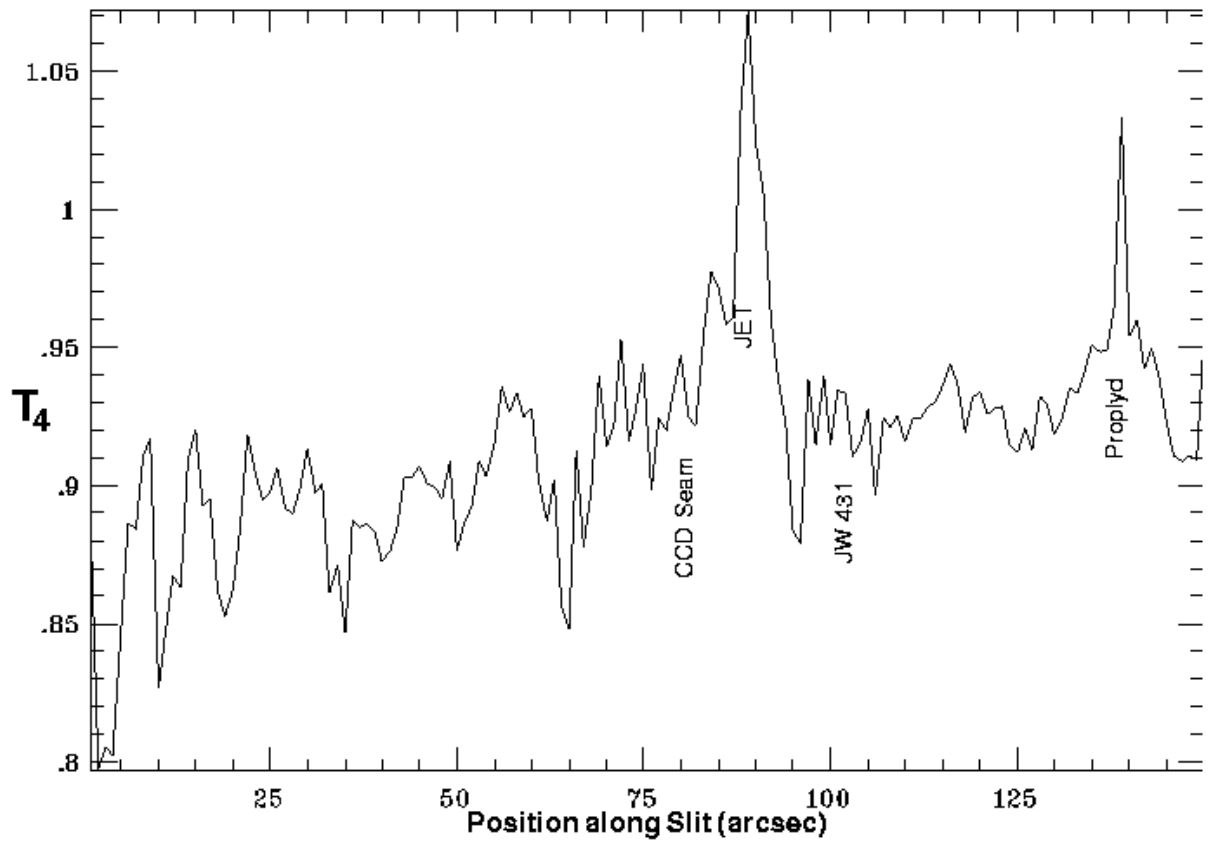


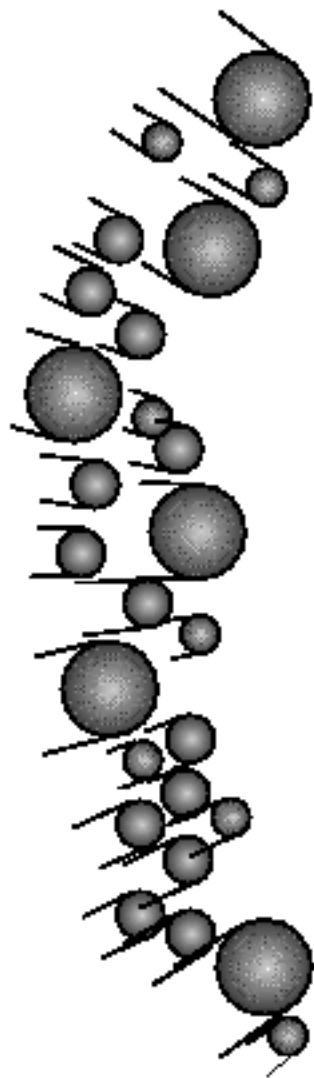












●  $\theta^1$  Ori C